ELSEVIER

Journal of Magnetism and Magnetic Materials 200 (1999) 470–497

Journal of magnetism and magnetic materials

www.elsevier.com/locate/jmmm

Exploring the microscopic origin of magnetic anisotropies with X-ray magnetic circular dichroism (XMCD) spectroscopy

J. Stöhr*

IBM Research Division, Almaden Research Center, 650 Harry Road, San Jose, CA 95120-6099, USA

Received 11 February 1999; received in revised form 13 April 1999

Abstract

Symmetry breaking and bonding at interfaces leads to a variety of anisotropy phenomena in transition metal sandwiches and multilayers. The charge density, the spin density and the orbital moment become anisotropic. These effects can be studied by the X-ray magnetic circular dichroism (XMCD) technique which senses the local anisotropy of charge, spin and angular momentum around an atom that is excited by the absorption of polarized X-rays. Here we briefly review the principles of the technique and then apply it to the study of the thickness-dependent electronic and magnetic properties of a Co film sandwiched between Au. The experimental results are compared to those obtained by electronic structure calculations for a free Co monolayer and a Co monolayer sandwiched between Au. In particular, a simple ligand field model is developed which allows one to visualize the origin of the magnetocrystalline anisotropy in terms of the preferred direction of the orbital moment, corresponding to the direction of maximum size. The model supports the intuitive picture that the orbital moment on an atom becomes anisotropic through quenching effects by the anisotropic ligand fields of the neighbors. © 1999 Elsevier Science B.V. All rights reserved.

Keywords: Anisotropy; Symmetry breaking; X-rays; Monolayers

1. Introduction

Transition metal thin films and surfaces may exhibit a variety of interesting magnetic phenomena such as enhanced spin and orbital magnetic moments [1–10], or enhanced magnetic anisotropies [11], e.g. perpendicular magnetic anisotropy (PMA) [12–16]. Such effects have their microscopic origin in the reduced symmetry experienced by magnetic atoms near interfaces or surfaces. Of particular interest from a technological point of view is the large PMA often found in artificially layered structures or the large perpendicular or in-plane uniaxial anisotropies in chemically ordered alloys with superlattice structures [17–20]. Such systems are also of great scientific interest in that they allow the exploration of one of the most important yet still poorly understood magnetic phenomena, the origin of magnetocrystalline anisotropy (MCA). Historically, it has been difficult to obtain a clear picture of the origin of the MCA because of its small size [21]. Even today the easy [1 1 1] magnetization direction of bulk FCC Ni cannot be accounted for by means of electronic structure calculations [22]. Van Vleck [23] first proposed the MCA to arise from the spin–orbit

* Tel.: + 001-408-927-2461; fax: + 001-408-927-2100.
E-mail address: stohr@almaden.ibm.com (J. Stöhr)

0304-8853/99/$ - see front matter © 1999 Elsevier Science B.V. All rights reserved.
PII: S0304-8853(99)00407-2

interaction which couples the isotropic spin moment to the lattice. In todays electronic structure calculations the magnetocrystalline anisotropy energy corresponds to the largest difference of the spin–orbit energy when the sample is magnetized along two different crystallographic directions. In the absence of shape anisotropy effects, the two directions then define the 'hard' versus the 'easy' magnetization directions.

In general, the complexity of electronic band-structure calculations impedes simple physical insight. In the case of layered thin films, however, the inherent in-plane/out-of-plane asymmetry and the resulting enhancement of the MCA by orders of magnitude [24] suggest exploration of a different, more intuitive, concept based on anisotropic bonding or ligand fields, as previously suggested by Wang et al. [25,26]. In addition, it is difficult to picture the origin of 'energy anisotropy'. Since our visualization of magnetism is closely related to magnetic moments it would be preferable to cast anisotropy concepts in terms of 'moment anisotropies'. In the present paper we will explore such 'ligand field' and 'moment' concepts.

The opportunity to directly observe the MCA as an anisotropy of the orbital moment, first suggested by Bruno [11,24], comes from the development of a powerful new magnetics technique called X-ray magnetic circular dichroism (XMCD) spectroscopy. The technique was pioneered by Schütz and coworkers in 1987 [27] and over the last ten years has been developed both experimentally [4,8, 28–37] and theoretically [5,6,38–45] into a quantitative magnetometry tool. It has several capabilities not afforded by traditional magnetics techniques [46]. Its foremost strengths are the element-specific, quantitative separation and determination of spin and orbital magnetic moments and their anisotropies. These capabilities are highlighted in the present paper. Other strengths, which will not be further discussed here, are its chemical sensitivity [16,47], its ability to identify moment orientations in ultrathin films and monolayer magnetic materials [48] which leads to its element-specific magnetic imaging capability [49], its ability to obtain element specific AC susceptibilities [50] and magnetization loops [51], and its sub-monolayer sensitivity [33,52,53].

The structure of the paper is as follows. The principles of XMCD spectroscopy will be reviewed in Section 2. In Section 3 XMCD results for a Au/Co/Au wedge with Co thickness ranging from 3 to 12 layers will be presented. In Section 4 the origin of anisotropy effects is discussed in terms of electronic structure calculations and a simple ligand field model. The XMCD results are discussed in terms of theoretical expectations in Section 5. Conclusions are presented in Section 6.

2. XMCD spectroscopy

2.1. XMCD spectroscopy in 3d transition metals

Here we shall briefly review the principles of XMCD spectroscopy. For more detailed accounts the reader is referred to earlier works [54–56]. The magnetic properties of the 3d transition metals are mainly determined by their d valence electrons [57,58]. In the ferromagnets Fe, Co and Ni the d shell becomes increasingly filled, resulting in a decreasing number of d holes, N. The spin magnetic moment due to the exchange interaction is simply the difference between the number of spin-up and spin-down holes, $m_s = -2\langle S_z\rangle\mu_B/\hbar = (N_\uparrow - N_\downarrow)\mu_B$. The orbital moment $m_o = -\langle L_z\rangle\mu_B/\hbar$ arises from the spin–orbit interaction which is significantly smaller ($\sim$50 meV) than the exchange interaction ($\sim$1 eV) and the 3d bandwidth (a few eV). Therefore, the orbital moment (e.g. $m_o = 0.14\ \mu_B$ for Co) is much smaller than the spin moment (e.g. $m_s = 1.64\ \mu_B$ for Co).

The properties of 3d-electrons are best probed in an X-ray absorption experiment by excitation of 2p core electrons to unfilled 3d states as illustrated by a simple one-electron picture[1] in Fig. 1a. In

[1] The one-electron diagram shown in Fig. 1 is misleading, especially to the photoemission community, in that it depicts the spin–orbit splitting of the p core shell as an 'initial state' effect. In the proper description based on a *configuration picture*, an atom is excited from a ground or initial state configuration to an excited or final state configuration. While in general the one electron and configuration pictures are not equivalent, equivalence does exist for the case of a d^9 ground state, as discussed in Ref. [54]. This, in fact, justifies the use of the one electron model.

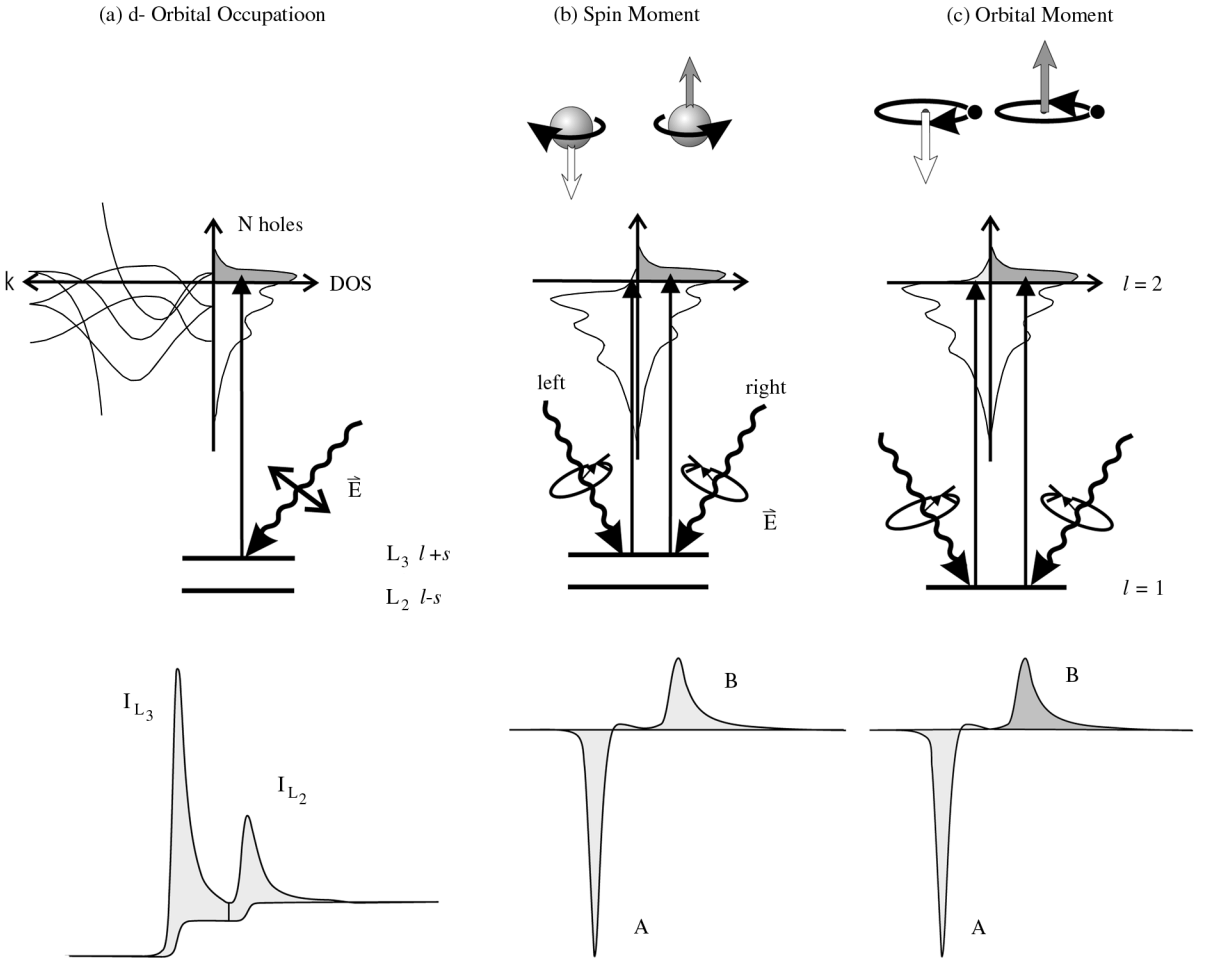

Fig. 1. (a) Electronic transitions in conventional L-edge X-ray absorption, (b) and (c) X-ray magnetic circular dichroism, illustrated in a one-electron model. The transitions occur from the spin–orbit split 2p core shell to empty conduction band states above the Fermi level. In conventional X-ray absorption the transition intensity measured as the white line intensity $I_{L_3} + I_{L_2}$ is proportional to the number of d holes, N. By use of circularly polarized X-rays the spin moment (b), and orbital moment (c), can be determined from the dichroic difference intensities A and B, as explained in the text.

principle, L-edge X-ray absorption spectra contain contributions from both $p \rightarrow d$ and $p \rightarrow s$ transitions, but in practice the $p \rightarrow d$ channel dominates by a factor > 20 [59]. The sum of the white line intensities, denoted I_{L_3} and I_{L_2}, respectively, is directly proportional to the number of d holes. This correlation follows from one of the several intensity sum rules [38,39,41] to be discussed below. The use of circularly polarized X-rays opens the door for magnetic studies. The underlying physics is most easily understood in the following two-step picture [54,55].

In the *first step*, right or left circularly polarized photons transfer their angular momentum, $\hbar$ and $-\hbar$, respectively, to the excited photoelectron. If the photoelectron originates from a spin–orbit split level, e.g. the $p_{3/2}$ level (L_3 edge), the angular momentum of the photon can be transferred in part to the spin through the spin–orbit coupling. Right circularly polarized photons transfer the opposite

momentum to the electron than left circularly polarized photons, and hence photoelectrons with opposite spins are created in the two cases. Since the $p_{3/2}(L_3)$ and $p_{1/2}(L_2)$ levels have opposite spin-orbit coupling ($l + s$ and $l - s$, respectively), the spin polarization will be opposite at the two edges. In the first (absorption) step, 'spin-up' and 'spin-down' are defined relative to the photon helicity or photon spin, which is parallel (right) or antiparallel (left) to the X-ray propagation direction. The handeness of circularly polarized light is not uniquely defined. We follow Feynman and the convention used in particle physics. See Ref. [60].

The magnetic properties enter in the *second step*. Here the spin-split valence shell acts as a detector for the spin of the excited photoelectron. The quantization axis of the detector is given by the magnetization direction which, for maximum dichroism effect, needs to be aligned with the photon spin direction. As illustrated in Fig. 1 we shall denote the differences of the white line intensities recorded with right and left circular polarization, i.e. the XMCD intensities, as A (L_3 edge) and B (L_2 edge), respectively. Note that A and B have opposite sign, reflecting the opposite spin–orbit coupling of the $p_{3/2}$ and $p_{1/2}$ levels. A powerful sum rule [39] links the spin moment quantitatively to the measured intensity $A - 2B$, as discussed below.

Similarly, if the d valence shell possesses an orbital moment, as shown in Fig. 1c, it will act as an orbital momentum detector for the excited photoelectron. By summing over the L_3, i.e. $(l + s)$, and L_2, i.e. $(l - s)$, intensities it is apparent that the spin s is eliminated and one measures the orbital moment of the valence shell, as schematically shown in Fig. 1c. This is expressed by the orbital moment sum rule [38] which links the orbital moment in the d shell to the dichroism intensity $A + B$.

In the above discussion we have assumed that the magnetization direction is fixed so that the XMCD intensity is the difference intensity, obtained for two X-ray helicities. It is easy to show that it is equivalent to fix the X-ray helicity and switch the magnetization direction [54].

2.2. Probing anisotropic charge and magnetic properties

So far we have implicitly assumed that the white line and dichroism intensities do not depend on the sample orientation relative to the X-ray wave vector or polarization. This is a rather good approximation for the *bulk* 3d transition metals which have high symmetry lattices (FCC, BCC or HCP) and hence the bonding and charge distribution is rather isotropic. In the following, we shall use a Cartesian coordinate system with the z-axis along the surface normal and assume uniaxial symmetry about z. If one describes the electronic band states in terms of basis functions consisting of the five d orbitals [61,62], d_{xy}, d_{xz}, d_{yz}, $d_{x^2-y^2}$, and $d_{3z^2-r^2}$, one may define d-orbital projected quantities after summing over the Brillouin zone (BZ). In particular, one obtains a density of states (DOS) for each d-orbital.

For bulk FCC transition metals one may distinguish bands derived from the $e_g(d_{x^2-y^2}$ and $d_{3z^2-r^2})$ and $t_{2g}(d_{xy}$, d_{xz} and $d_{yz})$ manifolds. The e_g and t_{2g} manifolds, respectively, possess a nearly isotropic charge density (i.e. have no quadrupole moment) and therefore, the total charge density in the atomic cell will also be nearly isotropic. Similarly, the spin density and the orbital moment will be rather isotropic. For ultra thin films or surfaces with uniaxial symmetry about the surface normal one may group the d-orbitals into in-plane ($d_{x^2-y^2}$ and d_{xy}) and out-of-plane (d_{xz}, d_{yz}, and $d_{3z^2-r^2}$) manifolds and define averaged in-plane and out-of-plane DOSs. This is illustrated in Fig. 2a for a free Co monolayer using the theoretical results of Daalderop [55,63] as a guide. It is seen that for a Co monolayer the out-of-plane DOS is narrower than the in-plane DOS because of smaller overlap of the out-of-plane (π bonding) relative to the in-plane (σ bonding) orbitals. The out-of-plane DOS exhibits more holes ($N^{\perp} = N^{xz} = N^{yz} = N^{3z^2-r^2}$) per orbital than the in-plane DOS ($N^{\parallel} = N^{xy} = N^{x^2-y^2}$). The DOSs lead to a slightly anisotropic charge (hole) distribution which is largest along the surface normal as schematically shown on the right side of Fig. 2a. The total number of d holes is given by $N = 2N^{\parallel} + 3N^{\perp}$, and is isotropic by definition.

From the spin resolved DOSs we can obtain the spin moments for each d-orbital. Per definition the

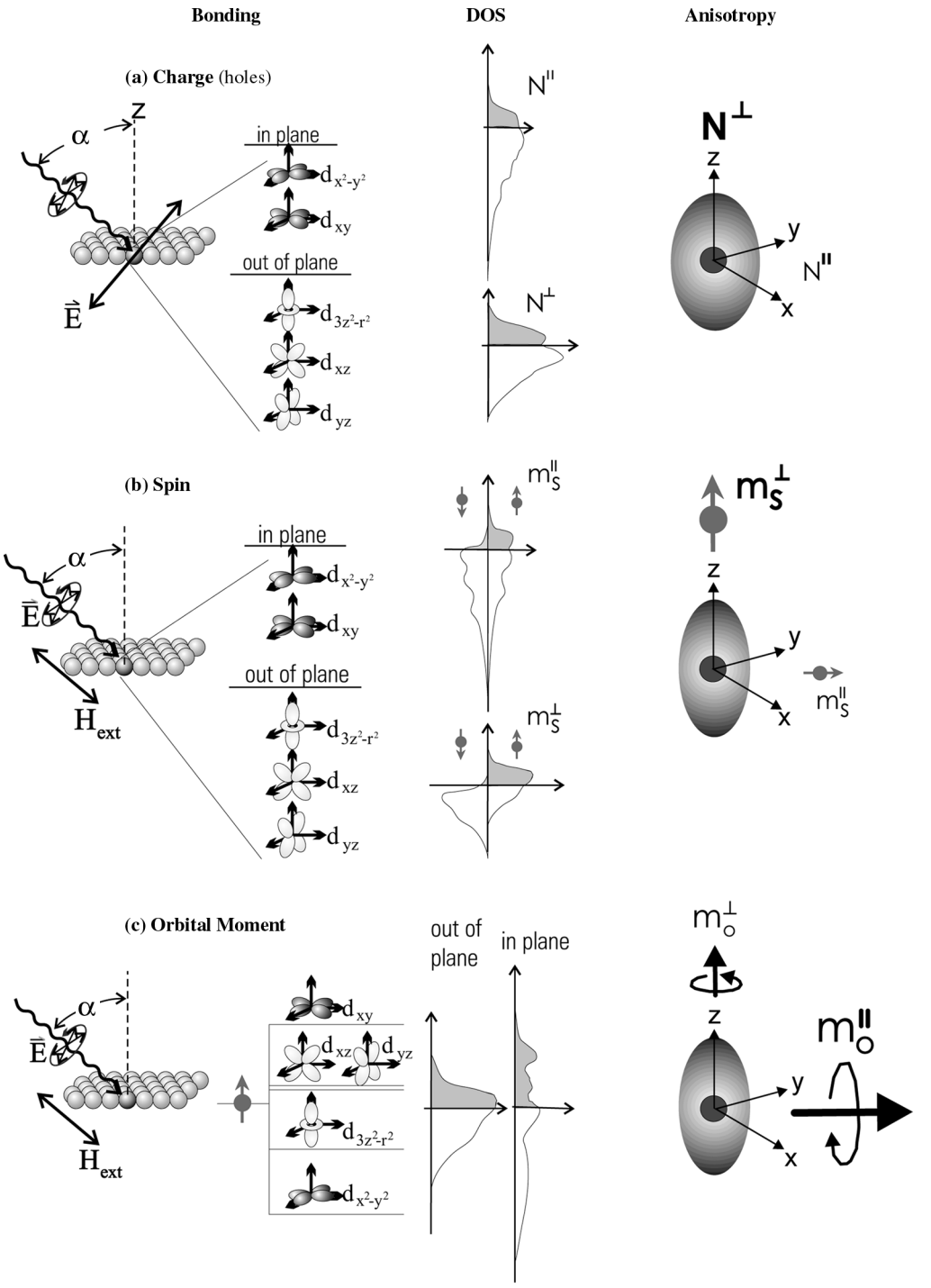
Bonding
DOS
Anisotropy
(a) Charge (holes)
z
α
in plane
$d_{x^2-y^2}$
d_{xy}
out of plane
$d_{3z^2-r^2}$
d_{xz}
d_{yz}
$\vec{E}$
$N^{\parallel}$
$N^{\perp}$
$N^{\perp}$
z
y
x
$N^{\parallel}$
(b) Spin
$m_s^{\parallel}$
$m_s^{\perp}$
$m_s^{\perp}$
z
y
x
$m_s^{\parallel}$
H_{ext}
(c) Orbital Moment
out of plane
in plane
$m_o^{\perp}$
$m_o^{\parallel}$
z
y
x

spin moment is the difference between the number of electrons in the majority band and the minority band. Neglecting hybridization effects between d electrons with the s and p electrons [6] one may also define the spin moment as the difference between the number of *holes* in the minority band and the majority band (note opposite sign) so that, with the definition of Fig. 1b and Fig. 2b, $m_s^i = (N_\uparrow^i - N_\downarrow^i)\mu_B$ for each d_i orbital. As shown in Fig. 2b for a Co monolayer the out-of-plane ($m_s^\perp = m_s^{xz} = m_s^{yz} = m_s^{3z^2-r^2}$) spin moment is found to be larger than the in-plane ($m_s^\parallel = m_s^{xy} = m_s^{x^2-y^2}$) one. The total isotropic spin moment is given by $m_s = 2m_s^\parallel + 3m_s^\perp$. In the transition metals Fe, Co and Ni there is a close correspondence between the anisotropy of charge and spin because the majority band is nearly full, as indicated in Figs. 2a and b. In practice, the anisotropy of the spin density is found to be larger than in the charge density because opposite minority and majority band contributions enhance the difference [55,63].

While the anisotropy of the charge and the spin is determined by the *filling* of the in-plane and out-of-plane sub-bands, i.e. the number of holes, the orbital moment anisotropy greatly depends on the in-plane versus out-of-plane *bandwidth* as illustrated in Fig. 2c. The orbital moment arises mainly from the minority band since a filled band has no net orbital moment. Its value is determined by the average bandwidth W which determines the average separation of the filled and empty minority band states that are mixed by the small spin–orbit interaction. A perturbation treatment gives $m_o \propto \xi/W$, where $\xi \sim 70$ meV is the spin–orbit coupling constant. Because the orbital moment direction is perpendicular to the plane of the orbiting hole or electron the in-plane moment $m_o^\parallel$ is determined by the out-of-plane orbitals and their bandwidth. The smaller out-of-plane bandwidth therefore leads to a larger in-plane orbital moment as indicated on the right side of Fig. 2c.

The polarized nature of X-rays allows one to quantitatively probe the various electronic and magnetic anisotropies, as discussed below.

2.3. Sum rules

2.3.1. Charge

Polarized X-rays are intrinsically anisotropic. For linearly polarized X-rays the electric field vector $\boldsymbol{E}$ defines a direction (axis) in space and right- and left-handed circularly polarized photons are characterized by a helicity vector which points either into the X-ray propagation direction $\boldsymbol{k}$ or along $-\boldsymbol{k}$. This anisotropy of polarized X-rays leads to a search light effect and allows the detection of anisotropic charge and moment distributions in magnetic thin films. Three sum rules relate the measured intensities I_{L_3}, I_{L_2}, A and B, defined in Fig. 1, to the electronic and magnetic properties of the sample. The first sum rule is related to the charge distribution and is given by [41],

$$[I_{L_3} + I_{L_2}]_\alpha = C(N + N_Q^\alpha), \tag{1}$$

where C is the square of the $p \rightarrow d$ radial transition matrix element and has a value of about 10 Mb eV [56]. We have characterized the anisotropy by an index α that specifies the orientation of $\boldsymbol{E}$ (linear polarization) or $\boldsymbol{k}$ (circular polarization). In the following α may either denote the coordinate axes x, y or z or the polar angle from the z-axis as defined in Fig. 2. Eq. (1) correlates the polarization dependent white line intensity with the total number of d holes $N = 2N^\parallel + 3N^\perp$ and a quadrupole term N_Q^α which expresses the anisotropy of the charge density in the unit cell [41]. The origin of this term is discussed in more detail in Appendix A. The sum rule expression $N + N_Q^\alpha = N_{eff}$ can be

Fig. 2. Illustration of the origin of charge, spin and orbital moment anisotropies in an ultrathin film using a free Co monolayer as an example [63]. (a) The bonding anisotropy is reflected by different densities of states for the in-plane and out-of-plane d orbitals. This leads to different numbers of unoccupied states above the Fermi level, i.e. the number of in-plane $N^\parallel$ and out-of-plane $N^\perp$ holes, as shown shaded. The total number of d holes $N = 2N^\parallel + 3N^\perp$, is isotropic per definition. (b) Same as (a) for the spin-resolved densities of states. The total spin moment, $m_s = 2m_s^\parallel + 3m_s^\perp$, is isotropic per definition. (c) Origin of the orbital magnetic moment illustrated in a d-orbital based bonding model [55]. If the bonding is anisotropic, as in the case of a multilayer, the energetic splitting between the in-plane and out-of-plane d orbitals will be different. In the presence of spin–orbit coupling the resulting orbital moment will be anisotropic.

written as a linear combination of $N^{\parallel}$ and $N^{\perp}$ [55]. For linear polarization α specifies the $\boldsymbol{E}$ direction and $\alpha = 0^{\circ}$ corresponds to $\boldsymbol{E} \perp z$ and $\alpha = 90^{\circ}$ corresponds to $\boldsymbol{E} \parallel z$ (see Fig. 2a) and we obtain

$$\begin{aligned} &\boldsymbol{E}\perp z: \quad N_{\mathrm{eff}} = 2N^{\perp} + 3N^{\parallel}, \\ &\boldsymbol{E}\parallel z: \quad N_{\mathrm{eff}} = 5N^{\perp}. \end{aligned} \tag{2}$$

For circular or plane polarization α specifies the $\boldsymbol{k}$ direction and $\alpha = 0^{\circ}$ corresponds to $\boldsymbol{k} \parallel z$ and $\alpha = 90^{\circ}$ corresponds to $\boldsymbol{k} \perp z$ (see Fig. 2a), and we obtain

$$\begin{aligned} &\boldsymbol{k}\parallel z: \quad N_{\mathrm{eff}} = 2N^{\perp} + 3N^{\parallel}, \\ &\boldsymbol{k}\perp z: \quad N_{\mathrm{eff}} = 3.5N^{\perp} + 1.5N^{\parallel}. \end{aligned} \tag{3}$$

The term N_{Q}^{α} vanishes when an angular average is performed, $\frac{1}{3}\sum_{\alpha} N_{\mathrm{Q}}^{\alpha} = (N_{\mathrm{Q}}^{x} + N_{\mathrm{Q}}^{y} + N_{\mathrm{Q}}^{z})/3 = 0$. In this case the isotropic sum rule $I_{\mathrm{L}_3} + I_{\mathrm{L}_2} = CN$ is obtained.

2.3.2. Spin

For 3d transition metals the spin–orbit coupling is small and the charge distribution is not significantly altered if the spin is rotated by an external magnetic field. As a consequence the anisotropy of the spin density is related to that of the charge density. In the following, we shall assume that in all measurements the sample is magnetically saturated by a strong external magnetic field along the X-ray propagation direction. The spin sum rule [39] is then given by [41]

$$[A - 2B]_{\alpha} = -\frac{C}{\mu_{\mathrm{B}}}(m_{\mathrm{s}} + m_{\mathrm{D}}^{\alpha}) \tag{4}$$

and it closely resembles the charge sum rule [55]. The total number of holes, N, is simply replaced by the isotropic spin moment $m_{\mathrm{s}} = 2m_{\mathrm{s}}^{\parallel} + 3m_{\mathrm{s}}^{\perp}$, and the charge density term N_{Q}^{α} is replaced by a spin density term m_{D}^{α}, also called an intra-atomic magnetic dipole moment [39,41]. This term, discussed in more detail in Appendix B, is non-zero in anisotropic bonding environments and reflects the fact that the number of spins in the unit cell differs along different crystallographic directions. The sum rule term $m_{\mathrm{s}} + m_{\mathrm{D}}^{\alpha}$ is again given by contributions of the various d orbitals. For circular polarization $\alpha = 0^{\circ}$ corresponds to the X-ray wave vector $\boldsymbol{k} \parallel z$ and $\alpha = 90^{\circ}$ corresponds to $\boldsymbol{k} \perp z$ (see Fig. 2b) and we obtain

$$\begin{aligned} &\boldsymbol{k}\perp z: \quad m_{\mathrm{D}}^{\parallel} = m_{\mathrm{D}}^{x} = m_{\mathrm{D}}^{y} = 2(m_{\mathrm{s}}^{\perp} - m_{\mathrm{s}}^{\parallel}), \\ &\boldsymbol{k}\parallel z: \quad m_{\mathrm{D}}^{\perp} = m_{\mathrm{D}}^{z} = 4(m_{\mathrm{s}}^{\parallel} - m_{\mathrm{s}}^{\perp}) \end{aligned} \tag{5}$$

or equivalently,

$$\begin{aligned} &\boldsymbol{k}\perp z: \quad m_{\mathrm{s}} + m_{\mathrm{D}}^{\parallel} = 5m_{\mathrm{s}}^{\perp} \\ &\boldsymbol{k}\parallel z: \quad m_{\mathrm{s}} + m_{\mathrm{D}}^{\perp} = 6m_{\mathrm{s}}^{\parallel} - m_{\mathrm{s}}^{\perp}. \end{aligned} \tag{6}$$

Polarized X-rays therefore offer the capability of probing the angular distribution of the spins in the atomic cell, whereas conventional magnetometry only probes the integrated number of spins, i.e. the essentially isotropic spin moment per atom. The term m_{D}^{α} vanishes when an angular average is performed, $\frac{1}{3}\sum_{\alpha} m_{\mathrm{D}}^{\alpha} = 0$, and the isotropic sum rule $A - 2B = -Cm_{\mathrm{s}}/\mu_{\mathrm{B}}$ is obtained [41]. The angular average requires that in all measurements the sample is magnetically saturated by a strong external magnetic field along the X-ray propagation direction.

2.3.3. Orbital moment

The electronic states created by the crystal potential alone possess no orbital moment, since all d orbitals have a perfect balance of $\pm m_{\mathrm{l}}$ contributions (see Fig. 13 below) [55]. This balance is broken by the spin–orbit interaction which mixes different d orbitals in a way to produce a non-zero angular momentum [24,55], as illustrated in Fig. 2c. If the bonding is anisotropic, the d electron charge will be anisotropic. When the sample is magnetized in different directions, i.e. by rotating the spin moment by a sufficiently strong external magnetic field, an orbital moment arises from the clockwise/counterclockwise imbalance of orbital motion in the plane perpendicular to the spin quantization axis as a consequence of the spin–orbit coupling. Because of the anisotropic charge cloud, the orbital amplitudes will differ for different magnetization (spin moment) directions, and the orbital moment will be anisotropic. The direction of the orbital moment relative to the spin moment is given by Hund's third rule. For Fe, Co and Ni m_{o} and m_{s} are parallel because the d shell is more than half full. In the presence of an external magnetic field which is sufficiently large to magnetically saturate the sample, the orbital

moment m_o^α along the field direction α can be directly determined by use of the sum rule [38]

$$[A + B]_\alpha = -\frac{3C}{2\mu_B} m_o^\alpha. \quad (7)$$

2.4. Magic geometries

The quantities N_Q^α, m_D^α and m_o^α all depend on the measurement geometry, characterized by α. For multilayers with uniaxial geometry about the surface normal, two 'magic' geometries are particularly useful. The first one, suggested by Stöhr and König [41], allows one to determine the angle averaged quantities N, m_s, and $m_o = (m^\perp + 2m^\parallel)/3$ in a single measurement. Assuming circularly polarized light, it consists of a measurement with the photon spin and the external magnetic field (strong enough to saturate the sample), oriented at the magic angle $\alpha = 54.7^\circ$ from the surface normal (equal projections onto x-, y- and z-axis). The second one, due to Dürr and van der Laan [42], directly determines the size of the anisotropic magnetic terms $m_D^\perp - m_D^\parallel$ and $m_o^\perp - m_o^\parallel$. It consists of a 'forbidden geometry' measurement, where the photon spin is *perpendicular* to the external magnetic field (strong enough to saturate the sample), and the sample is at $\alpha = 45^\circ$ X-ray incidence.

3. Magnetic anisotropies in Au/Co/Au sandwiches

The microscopic origin of magnetic anisotropy in transition metals has been debated for more than 60 years [23]. Recently, the interest in this problem has become revived in conjunction with artificially made transition metal multilayers which exhibit perpendicular magnetic anisotropy (PMA) [12–14,64]. For example, PMA is observed when a thin Co film, a few atomic monolayers thick, is sandwiched between two transition metal films such as Au, Pt, Pd, In or Ni, as shown in Fig. 3. For such multilayers the easy magnetization direction deviates from the in-plane orientation observed for thicker (tens or hundreds on nanometers) Co films.

The case of perpendicular magnetic anisotropy is of considerable interest for technological applications such as magneto-optical recording [65]. It is clear that PMA is due to an intrinsic, i.e. magneto-crystalline, anisotropy mechanism strong enough to overcome the extrinsic macroscopic shape anisotropy, which favors an in-plane orientation of the magnetization [24], as discussed in detail in Section 4.1. The microscopic origin of the PMA has remained fuzzy, however. While it is clear now that the PMA is determined by the anisotropy of the spin–orbit energy, different mechanisms have been proposed to dominate. Some authors [21,63,66] have stressed the importance of band structure effects, especially of states close to the Fermi level which are strongly mixed by the spin–orbit interaction while others [25,26] have emphasized the importance of anisotropic bonding at interfaces which may be described by a ligand field model that averages out band effects. It has also been suggested that the increased spin–orbit interaction in 'heavy' ligands such as the 4d and especially the 5d transition metals is important through hybridization effects at interfaces [7,63].

In the following, we shall use the model staircase structure shown in Fig. 4a, to explore the microscopic origin of the magnetocrystalline anisotropy and how it leads to PMA. The Co/Au/Co staircase bridges the two structures shown in Fig. 3 and exhibits in-plane magnetic anisotropy at the thick end and PMA at the thin end.

3.1. Sample preparation

The Au/Co-staircase/Au sample was prepared by MBE (for details see Refs. [67–70]) using room temperature deposition of the metals in ultrahigh vacuum, with background pressures below 5×10^{-10} mbar during film growth. First, a 28 nm thick Au buffer is grown onto a float-glass substrate, which after annealing for 1 h at 175°C provides an atomically flat and fully (1 1 1) textured template. Subsequently, ten Co terraces of 2 mm width and thicknesses between 3 and 12 monolayers (ML) of Co are generated using a linear shutter at the low growth rate of 0.3 ML/min, and are finally capped with a ~ 9 ML thick Au layer. A schematic picture of the resulting Au/Co-staircase/Au sample is shown in Fig. 4a. The sample consists of ten Co terraces of 2 mm width ranging from 3 and 12 atomic layers, corresponding to thicknesses 6.15 Å $\leqslant t \leqslant$ 24.6 Å.

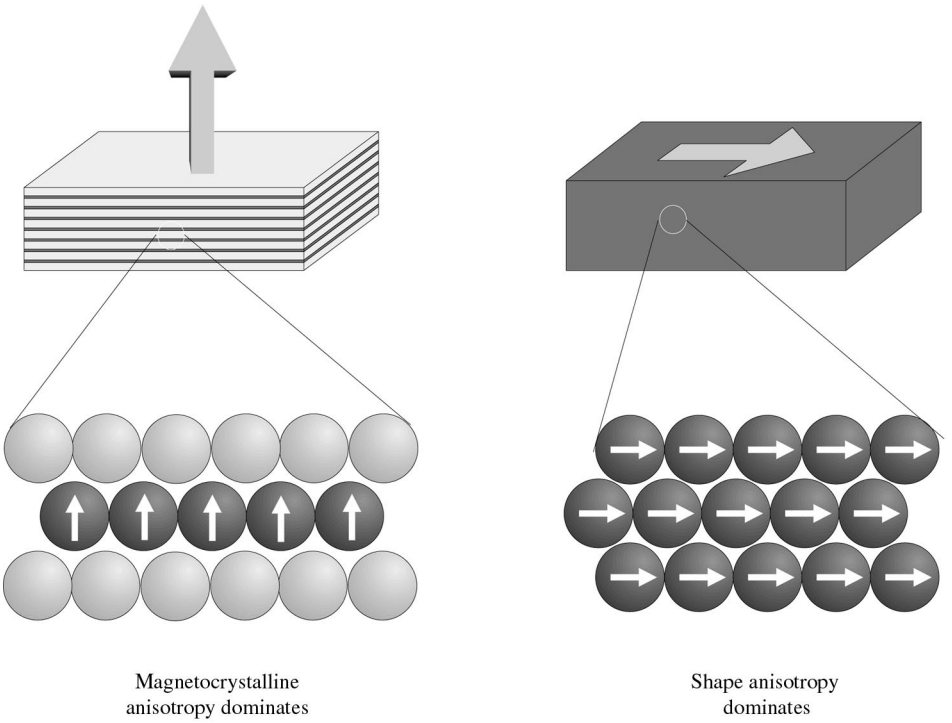

Fig. 3. Illustration of magnetic anisotropies in two often encountered cases. In magnetic films with a thickness exceeding about 2 nm the easy magnetization direction is typically found to be in-plane due to the dominance of the magnetostatic shape anisotropy. In multilayer systems, consisting of ultrathin alternating magnetic (sub-nanometer thickness) and non-magnetic layers, such as Co and Au, discussed in this paper, the easy axis may be out-of-plane due to the dominance of the spin–orbit derived magnetocrystalline anisotropy.

3.2. Kerr results

The Co staircase was characterized by angle-dependent polar Kerr hysteresis measurements in fields up to 20 kOe [7]. Plateaus in both the coercivity and the Kerr rotation confirmed its steplike structure as shown in Fig. 4b. The intrinsic energy anisotropy (per Co volume), K_1, was found to follow a $K_V + 2K_S/t$ dependence, as shown in Fig. 4c, with volume and surface anisotropy constants $K_V = 0.45$ MJ/m^3 and $K_S = 3.4$ MJ/m$^3 = 0.70$ mJ/m^2, respectively. By extrapolation we obtain for the energy anisotropy of a monolayer of Co sandwiched between Au $E_{so} = -7.3$ MJ/m$^3 = -5.1 \times 10^{-4}$ eV/atom. The size of K_V together with the observation of a second-order anisotropy constant $K_2 = 0.1$–0.2 MJ/m^3 are consistent with mostly hexagonal (0 0 0 1)Co. With these anisotropy constants, the transition from out-of-plane to in-plane anisotropy occurs at $t \approx 11$ ML [35].

3.3. XMCD measurements

XMCD measurements were performed at room temperature at the Stanford Synchrotron Radiation Laboratory (SSRL) on beamline 8-2. Circularly polarized X-rays were obtained by moving the pre-focusing mirror below the electron orbital plane, yielding a degree of polarization of $90 \pm 5\%$. The X-ray absorption was measured by the photocurrent from the sample [55] using right circularly polarized X-rays and switching the magnetization direction parallel and then antiparallel to the photon spin at each photon energy step.

The XMCD spectra were recorded in a 10 kOe external magnetic field oriented parallel to the X-ray

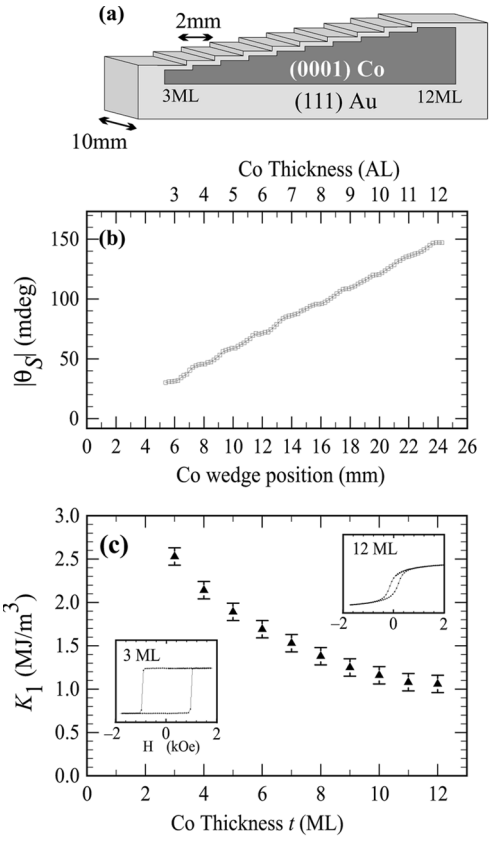

Fig. 4. (a) Schematic of the investigated Au/Co-staircase/Au sample. (b) Kerr rotation as a function of Co thickness. (c) Anisotropy constant K_1, determined from the measured Kerr loops, as a function of Co thickness. The inset shows polar geometry Kerr hysteresis loops (magnetization measured in the out-of-plane direction) for 3 and 12 ML Co. The hysteresis loops show that at 3 ML, the easy axis is out-of-plane, and it rotates in-plane as the Co thickness increases to 12 ML.

propagation direction, at angles $\alpha = 0$ and 65° with respect to the surface normal of the sample. A high transmission grid, formed in shape of a cylinder, around the sample produced an electric bias field of $+200$ V to draw the photogenerated electrons from the grounded sample. This arrangement avoids experimental asymmetries in the presence of large magnetic fields [55].

Measurements for different Co thicknesses were performed by translating the sample along the wedge direction. The X-ray beam spot size was about 0.75 mm along the translation direction, assuring adequate spatial resolution for the 2 mm wide Co terraces.

3.4. XMCD results

Experimental XMCD results for two Co thicknesses, normalized to a per Co atom basis, are shown in Fig. 5 for X-ray incidence angles $\alpha = 0$ and 65° from the surface normal. While the spectra for 11 ML thickness look identical a difference is discernable in the intensity of the L_3 peak near 775 eV in the 4 ML spectra. The sum rule derived values for the number of d holes and the spin and orbital moments derived from the original data, corrected for electron yield saturation effects [71], are plotted in Fig. 6 as a function of Co thickness. A clear anisotropy is found for the orbital moment in the $\alpha = 0°$ relative to the $\alpha = 65°$ data at the thin edge of the Co wedge. A smaller anisotropy is found in the values derived from the spin sum rule, corresponding to $m_s + m_D^{\alpha}$, while no anisotropy is observed within experimental uncertainty for the values derived from the charge sum rule.

The anisotropy of the orbital moment, after correction for insufficient magnetic saturation of the sample in the applied field of 10 kOe and for the finite X-ray incidence angle ($\alpha = 65°$) (see footnote 2 and Ref. [72]), is shown in more detail in Fig. 7. Here we have plotted the orbital moments $m_o^{\parallel}$ and $m_o^{\perp}$, the average moment $m_o = (2m_o^{\parallel} + m_o^{\perp})/3$ and the difference $\Delta m_o = m_o^{\perp} - m_o^{\parallel}$. The angle averaged orbital moment decreases in value with decreasing Co thickness, probably because of a reduced Curie temperature, and is approximately constant for $t \geqslant 6$ ML at the Co bulk value of $m_o = 0.14\,\mu_B$. At the thin end of the wedge the orbital moment is found to be strongly anisotropic, with a value $\Delta m_o = 0.22\,\mu_B$ at the 3 ML Co step. Δm_o decays rapidly and becomes smaller than the experimental error for thicknesses larger than 7 ML. The measured data in Fig. 7c appear to deviate somewhat from a $1/t_{Co}$ behavior (dashed line) although the statistical accuracy of the data is insufficient to draw a definite conclusion. Instead, two different fits (linear and exponential) were used (see Fig. 7c) to estimate the orbital moment anisotropy for 1 ML Co sandwiched between Au, $m_o^{\perp} - m_o^{\parallel} = (0.37 \pm 0.05)\,\mu_B$/atom.

Fig. 8a shows the anisotropy of the spin density with Co thickness, after correction for insufficient magnetic saturation of the sample in the applied field of 10 kOe and for the finite X-ray incidence

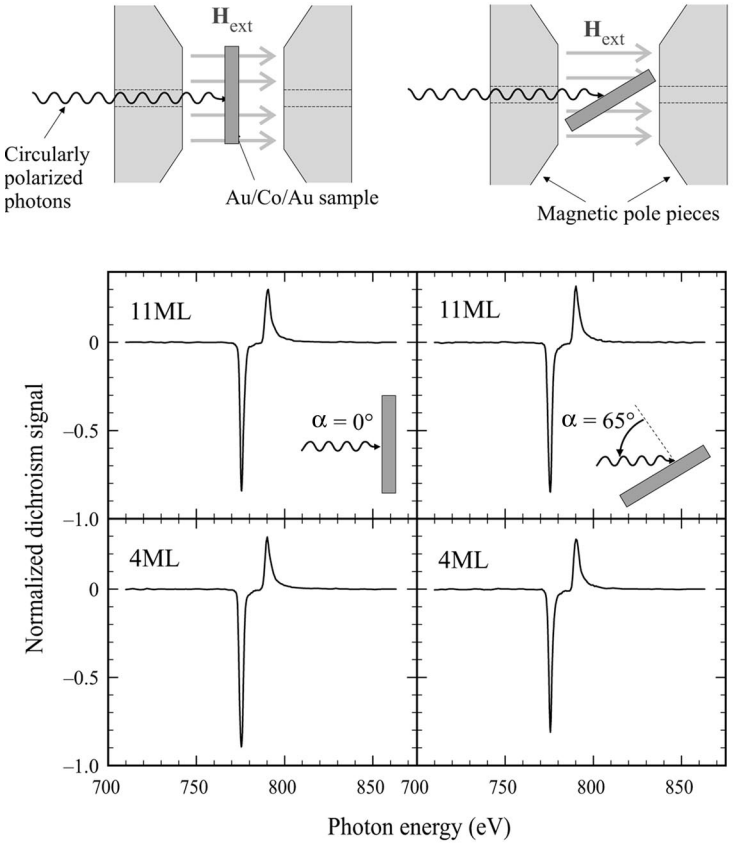

Fig. 5. Top: XMCD experimental setup for photon spin $\boldsymbol{P}$ at 0° (left) and 65° (right) incidence with respect to the sample normal. In our experimental setup, the external magnetic field was reversed such that it was either parallel or antiparallel to the photon spin for the XMCD absorption measurements. Bottom: Dichroism spectra at 4 and 11 ML Co at X-ray incidence angles of 65° (right) and 0° (left) from the surface normal.

angle ($\alpha = 65°$)[2] (for details see Ref. [72]). We also show the values for the average isotropic spin moment, m_s, derived by use of the angular average $\sum_\alpha m_D^\alpha = 0$, and the anisotropy of the dipole moment m_D^α. At the thin end of the wedge the average spin moment decreases by 15% from the bulk value of $m_s = 1.64\ \mu_B$ measured at the thick end of the wedge. The dipole moment anisotropy increases with decreasing Co thickness and amounts to $\Delta m_D = 0.22\ \mu_B$ at the 3 ML Co step. The fits in Fig. 8c give values $m_D^\perp = 0.44\ \mu_B$ and $m_D^\parallel = -0.22\ \mu_B$ for 1 ML Co sandwiched between Au. The anisotropy in the dipole moment tracks that of the orbital moment, indicating a close relationship between orbital and dipolar anisotropies.

[2] The measured anisotropic moments in the photon spin direction $\hat{\boldsymbol{P}}_\alpha \cdot \boldsymbol{m}_x = m_x^\alpha$ for $\alpha = 0$ and 65°, where x denotes either the orbital moment or the dipolar spin moment, have been converted into moments $m_x^\parallel$ and $m_x^\perp$ by means of the equation $m_x^\alpha = m_x^\parallel \sin\vartheta \sin\alpha + m_x^\perp \cos\vartheta \cos\alpha$, derived by Dürr et al. [94]. The equilibrium magnetization angle ϑ which lies between the applied field direction $\boldsymbol{H}_{ext} \| \hat{\boldsymbol{P}}_\alpha$ and the easy axis of magnetization, was obtained from the polar Kerr hysteresis loops $\theta_K^\alpha(H)$ measured at a field angle α in fields $\pm H_{ext}$, according to the relation $\theta_K^\alpha(10\,\text{kOe})/\theta_K^{\alpha=0°}(20\,\text{kOe}) = \cos\vartheta$ where a field of 20 kOe is assumed to be sufficiently strong to magnetize the Co film in the perpendicular direction for all Co thicknesses.

4. Origin of magnetic anisotropies

4.1. Dipolar anisotropy

The easy magnetization axis of a sample is determined by a competition between two anisotropy

mechanisms arising from the magnetostatic dipole–dipole coupling of the magnetization distributions within the individual atomic cells, i.e. the magnetic moment densities, and from the spin–orbit interaction [24]. In general, the magnetization distribution in the atomic cells contains spin and orbital contributions and it is not spherical but involves various multipoles. In the multipole expansion of the spin density[3] the largest (monopole) term, after integration over the atomic volume, corresponds to the magnetic spin moment. Since it arises from the exchange interaction the spin moment is intrinsically isotropic and magnetic anisotropy arises only from the preferred dipolar coupling between the atomic moments. The monopole term in the spin density therefore gives rise to the conventional dipole–dipole interaction between magnetic moments $\boldsymbol{m}_s$, located at the atomic positions in the lattice,

$$E_{\mathrm{dip-dip}} = \frac{\mu_0}{4\pi}\sum_{i\neq j}\frac{1}{r_{ij}^3}\left[\boldsymbol{m}_i\cdot\boldsymbol{m}_j - 3\frac{(\boldsymbol{r}_{ij}\cdot\boldsymbol{m}_i)(\boldsymbol{r}_{ij}\cdot\boldsymbol{m}_j)}{r_{ij}^2}\right]. \quad (8)$$

The summation is over all atomic dipoles $\boldsymbol{m}_i$ and $\boldsymbol{m}_j$, whose absolute values are given by the spin moment m_s. Every pair of dipoles is only counted once, and $\boldsymbol{r}_{ij}$ is the vector connecting the two moments. The next higher (quadrupole) term in the multipole expansion of the spin density reflects the lowest-order anisotropic spin distribution in the atomic cell and it gives rise to the intra-atomic magnetic dipole moment $\boldsymbol{m}_D$ discussed in conjunction with the spin sum rule (see also Appendix B). The orbital moment also contributes to the magnetization density in the atomic volume and its anisotropy is typically comparable to that of the intra-atomic magnetic dipole moment, as seen from Figs. 7 and 8. Since the anisotropies of m_o^α and m_D^α are much smaller than the spin moment m_s, in practice, the contributions of the anisotropic

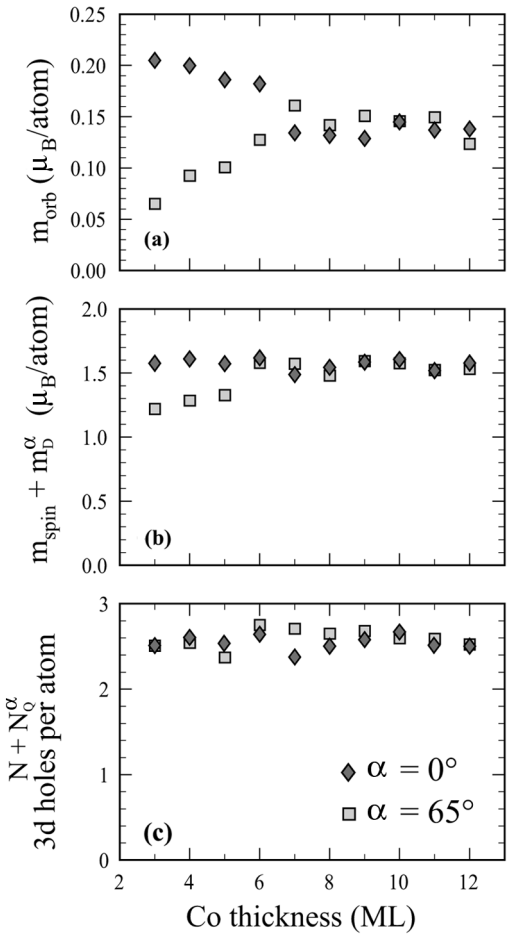

Fig. 6. Sum rule derived white line (a), spin moment (b), and orbital moment (c) values as a function of Co layer thickness for incidence angles $\alpha = 0$ and 65° from the surface normal of the circularly polarized X-rays. The data have been corrected for electron yield saturation effects [71].

m_o^α and m_D^α terms to the magnetostatic energy can be neglected and it is sufficient to consider the lowest-order magnetic dipole–dipole interaction given by Eq. (8).

Remembering that all moments are parallel because of the dominant exchange interaction, the dipole–dipole energy between two magnetic dipoles, for example, is smallest when both atomic moments align parallel along the internuclear axis. For a thin film the internuclear axes are preferentially oriented in the plane of the sample and the

[3] When the magnetization distribution in the unit cell is expanded in multipoles the dipole–dipole interaction has the general form of Eq. (8) but the size of the moments $\boldsymbol{m}_i$ is given by the multipole expansion $m_i = m_s + m_D^z/2 + \cdots$. The monopole term m_s gives Eq. (8), the quadrupole term $m_D^z/2$ makes a contribution of order $m_D^z/2m_s$.

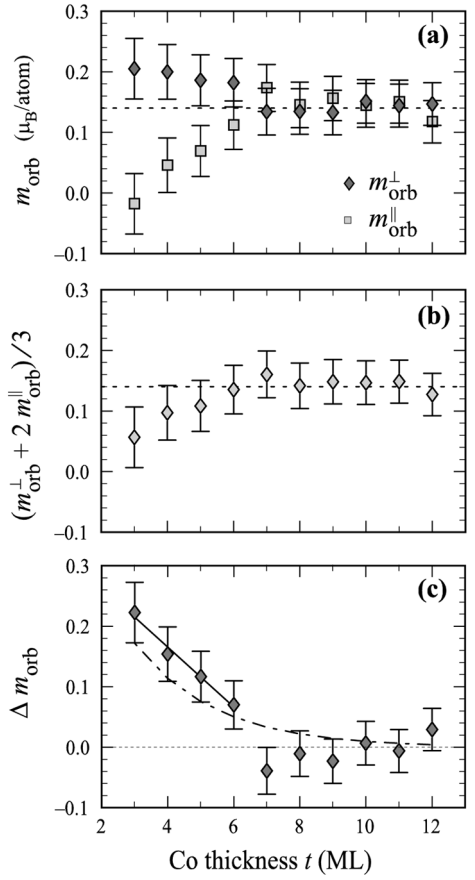

Fig. 7. XMCD analysis of $m_o^{\perp}$ and $m_o^{\parallel}$. (a) Orbital moments $m_o^{\perp}$ and $m_o^{\parallel}$. (b) The isotropic orbital moment $(m_o^{\perp} + 2m_o^{\parallel})/3$. (c) The orbital moment anisotropy, $\Delta m_o \equiv m_o^{\perp} - m_o^{\parallel}$. The linear fit to 3–6 ML data (solid line) and an approximate exponential fit to all of the data (3–12 ML; dot–dashed line) give $\Delta m_o = -0.05 \times t + 0.36$ and $\Delta m_o = 0.59e^{-0.41 \times t}$, respectively.

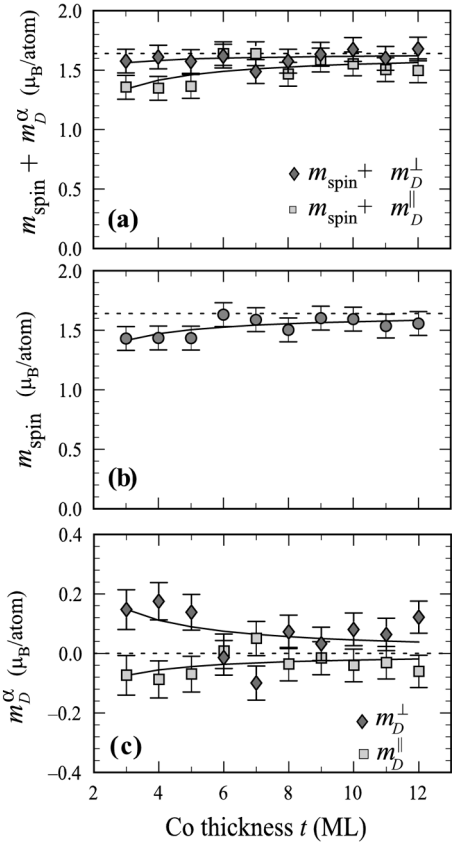

Fig. 8. XMCD sum rule results for $m_s + m_D^{\perp}$ and $m_s + m_D^{\parallel}$, plotted versus Co thickness t. (b) Isotropic spin moment m_s. The net spin moment decreases with decreasing Co thickness, due to the drop in Curie temperature. The curve fit shown is the function $m_s = 1.64 - (0.67/t)$. (c) Spin dipole moments $m_D^{\perp}$ and $m_D^{\parallel}$ with fits $m_D^{\perp} = (0.44/t)$ and $m_D^{\parallel} = -(0.22/t)$.

dipole energy is therefore minimized for an in-plane direction of the magnetic moment. For bulk materials the dipolar field may be decomposed into three contributions, a 'microscopic' component consisting of the contributions from the atomic dipoles on the actual lattice sites within a spherical volume, E_S, that arising from pseudo-charges on the surface of the sphere, E_L, and a 'macroscopic' component due to the demagnetizing field from pseudo-charges on the external sample surface, E_D, according to

$$E_{dip-dip} = E_S + E_L + E_D. \tag{9}$$

The dominant term, E_D, arising entirely from the demagnetizing field, is the well-known shape anisotropy, given by

$$E_D = -2\pi M_V^2, \tag{10}$$

where M_V is the volume magnetization. The other two terms depend on the crystallographic arrangement of the atoms in the sphere and therefore constitute a dipolar magnetocrystalline anisotropy. For Co, for example, the microscopic component is found to be negligible in size ($E_S + E_L \approx 4 \times 10^{-7}$ eV/atom) relative to the shape anisotropy ($E_D = 9.3 \times 10^{-5}$ eV/atom) [24].

For surfaces and ultrathin films the anisotropy may be calculated by a two-dimensional lattice sum [73]. Typical anisotropy energies are $\leqslant 5\times 10^{-5}$ eV/atom for a single ferromagnetic layer, smaller than those observed experimentally [24]. Therefore, the magnetocrystalline anisotropy, in general, and the PMA, in particular, cannot be accounted for by a dipolar anisotropy. Instead, they arise from spin–orbit coupling as suggested by Van Vleck [23].

4.2. Spin–orbit anisotropy

Todays electronic structure calculations account for Hund's first rule (maximum spin) by using the local spin-density approximation for the exchange splitting. However, such theories do not adequately account for Hund's second rule (maximum orbital momentum) and this deficiency leads to orbital moments that are too small. Eriksson et al. [57,74] have proposed an orbital enhancement term that leads to much better agreement between theory and experiment. Hund's third rule (total angular momentum) is accounted for by treating the spin–orbit interaction either fully relativistically [75,76] or by perturbation methods [11,21,25]. In particular, the small MCA energies correspond to the energetic difference obtained by two calculations with the spin direction chosen along two orthogonal crystallographic axes, corresponding to the easy and hard magnetization directions.

Owing to the complexity of electronic structure calculations it is difficult to obtain a simple physical picture that catches the essence of the magnetocrystalline anisotropy mechanism. For the bulk transition metals Fe, Co and Ni the crystal symmetries are high and the MCAs are extremely small (10^{-6} eV/atom) so that insight into the origin of the anisotropy mechanism is nearly impossible to obtain [21,22]. In contrast, the MCA in anisotropic systems like monolayers and multilayer systems is larger by orders of magnitude (10^{-4} eV/atom), suggesting a possible interpretation of the MCA based on symmetry breaking and asymmetric bonding at the magnetic surfaces or interfaces. Such an interpretation is supported by the preference for PMA in many multilayer systems, independent of the detailed crystallographic structure of the layers. A symmetry-based model has indeed been suggested by Wang et al. [25,26] who compared first principles band structure results with those obtained from a more intuitive ligand field model that accounts for the different in-plane and out-of-plane bonding at surfaces and interfaces. The ligand field approach used by Wang et al. was based on comparison of spin–orbit *energies* for in-plane versus out-of-plane orientations of the spin.

Bruno [11,24] has shown that under certain assumptions the anisotropy of the *spin–orbit energy* is directly related to the anisotropy of the *orbital moment* according to

$$\Delta E_{so} = C(m_o^{\parallel} - m_o^{\perp}), \tag{11}$$

where $C > 0$ is a proportionality constant. Bruno's work followed careful high field measurements of the anisotropy of the total (spin plus orbital) magnetic moment by Aubert, Rebouillat, Escudier and Pauthenet [77–80]. The relationship between the orbital moment and the magnetic anisotropy was also discussed in an early paper by Ducastelle and Cyrot-Lackmann [81]. We have used the definition that $\Delta E_{so} < 0$ if the easy axis is perpendicular to the surface and the orbital moment is larger in the easy direction than in the hard one.[4] Bruno's model leads to a particularly simple and beautiful picture for the origin of the MCA based on the anisotropy of the orbital moment. This is illustrated in Fig. 9, using concepts by Smit [82]. Consider a d electron in a free atom whose spin is oriented by an external magnetic field. The orbital momentum of the d electron circling about the spin direction can then take on values $-2 \leqslant \langle L_z \rangle \leqslant +2$, as depicted in Fig. 9. Let us now assume that, instead, the atom is bonded in a planar geometry to four other atoms with a negative charge as shown in Fig. 9. Now the orbiting electron will experience a Coulomb repulsion near the corners of the bonding square where the negative neighbor ions are located and the orbiting electron will form a standing wave by superposition of two oppositely travelling waves with $\pm L_z$, with charge maxima away from the four corners. One may say that the in-plane orbit of the

[4] Note that $\Delta E_{so} = -K_1$ with the convention $E_{so} = K_0 + K_1 \sin^2\theta$ used by Bruno [24].

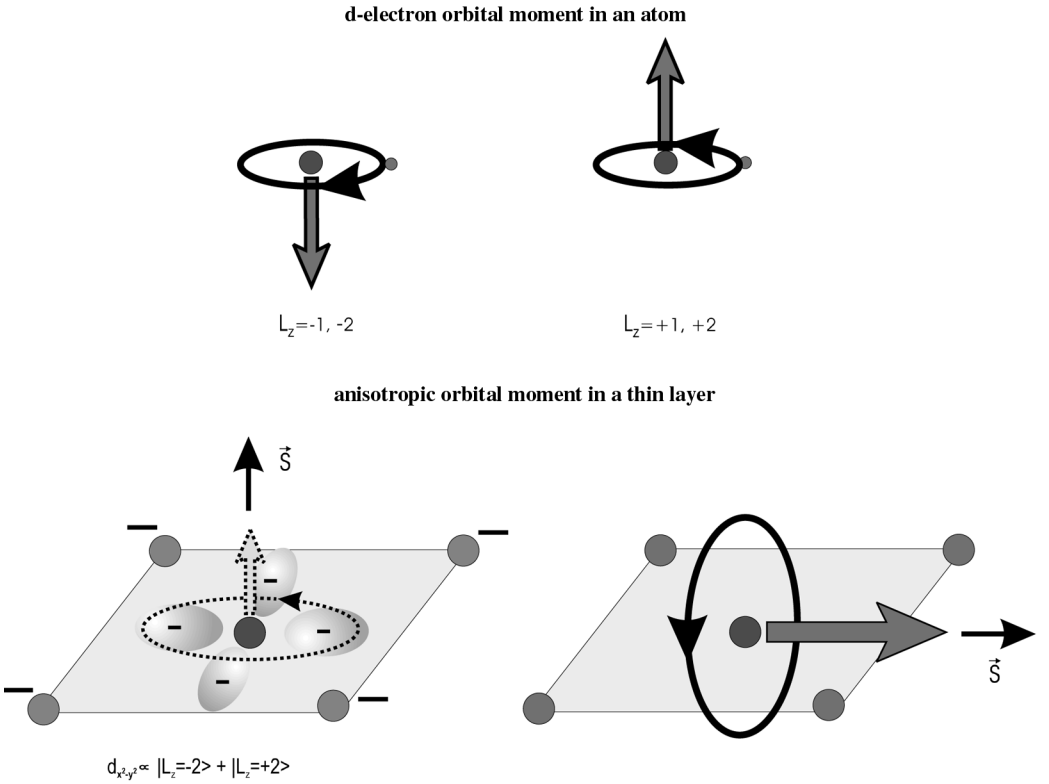

Fig. 9. Directional quenching of the orbital momentum of an atom by ligand field effects in a thin film, as discussed in the text.

electron is broken up through the formation of molecular orbitals (e.g. a $d_{x^2-y^2}$ orbital in our case). Therefore, the corresponding orbital momentum along the normal of the bonding plane, will be quenched. The orbital motion perpendicular to the bonding plane will be less disturbed owing to the lack of neighbor ions and the corresponding in-plane orbital momentum remains largely unquenched. The simple model pictured in Fig. 9 therefore relates the anisotropy of the orbital moment of an atom to the anisotropy of the bonding environment. For a free monolayer the orbital momentum (or moment) is predicted to be larger in the bonding plane than perpendicular to it, and for the case of stronger out-of-plane bonding, e.g. for a multilayer, the orbital moment would be larger in the out-of-plane direction.

In the following, we shall explore the origin of the PMA in Au/Co/Au more quantitatively, using the concepts of anisotropic bonding and orbital anisotropy.

4.2.1. From band structure to ligand field model

The question arises whether the simple model shown in Fig. 9 is qualitatively correct for thin metal films. One might argue that the simple point charge model or the concept of directional bonding does not apply for metallic systems and that the model therefore has no validity. However, first principles band structure calculations indeed provide the basis for anisotropic bonding in monolayer and multilayer systems. For example, Fig. 10 taken from Daalderop et al. [63] clearly shows the different bandwidth associated with the in-plane d_{xy} and $d_{x^2-y^2}$ orbitals relative to the out-of-plane d_{xz}, d_{yz}, and $d_{3z^2-r^2}$ orbitals for a free Co monolayer. As expected from simple arguments [25,26], the overlap of the in-plane orbitals (σ bonding) leads to

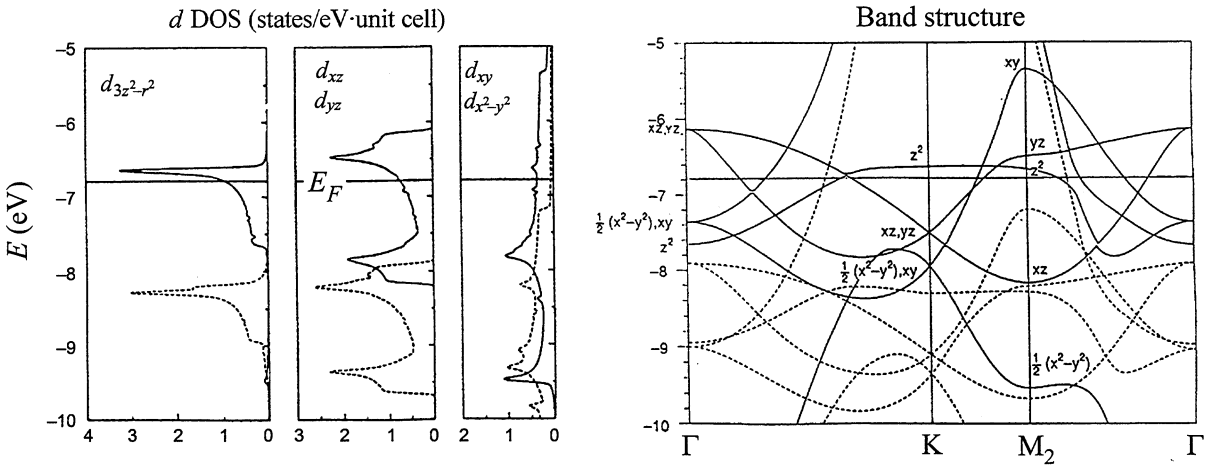

Fig. 10. Density of states and band structure of a free-standing Co(1 1 1) monolayer, calculated by Daalderop et al. [63]. (a) Majority- (dashed) and minority-spin (solid) orbital projected density of states for $m = 0$ ($d_{3z^2-r^2}$), $|m| = 1$ (d_{xz}, d_{yz}), and $|m| = 2$ ($d_{x^2-y^2}$ and d_{xy}). The 'out-of-plane' orbitals (i.e. $|m| = 0, 1$) have a narrower bandwidth than the 'in-plane' orbitals (i.e., $|m| = 2$). (b) Majority- (dashed) and minority-spin (solid) band structure of Co monolayer.

a larger bandwidth, relative to that for the less overlapping out-of-plane orbitals (π bonding). In contrast, when the Co monolayer is sandwiched between Au layers, the strong out-of-plane bonding significantly increases the out-of-plane bandwidth. This is shown in Fig. 11, where the density of states (DOS) for the Co $d_{3z^2-r^2}$ orbital in a free Co monolayer [63], taken from Fig. 10, is compared to that calculated by Újfalussy et al. [83] for the same orbital in a Au/Co/Au sandwich. Figs. 10 and 11 suggest that an anisotropic bonding model may be used for the description of the electronic structure of a free or sandwiched ultrathin magnetic layer. In the following we shall develop such a model for the calculation of the orbital moment.

We can schematically represent the band structure results for a free Co monolayer, shown in Fig. 10 by the simple DOS model shown in Fig. 12. Here the majority (spin down) band is assumed to be filled, and we shall assume the minority band to be half-filled as obtained by the band structure results for bulk and monolayer Co [26,63]. We shall distinguish contributions from in-plane and out-of-plane d states. The in-plane d bandwidth is larger and the empty and filled states have an average separation $2V_{\|}$. The narrower out-of-plane d band

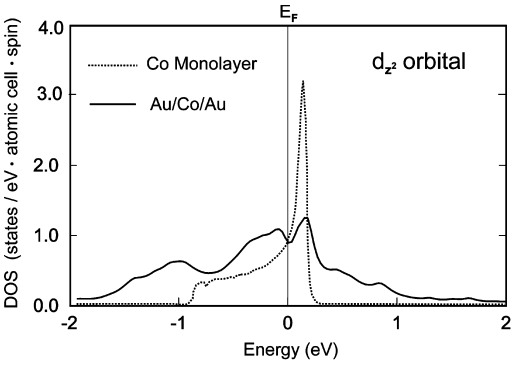

Fig. 11. Density of states for the $d_{3z^2-r^2}$ orbital in a Co monolayer taken from Daalderop et al. [63] and for a Co monolayer sandwiched between Au [structure Au(1 1 1)/Co(1 ML)/Au(2 ML)] taken from Újfalussy et al. [83].

exhibits an average separation between the empty and filled states of $2V_{\perp}$. In our model, shown in Fig. 12, we further assume that the DOSs for the in-plane d_{xy} and $d_{x^2-y^2}$ orbitals are the same. We make the same assumption for the out-of-plane d_{xz}, d_{yz} orbitals and assume that the DOS for the $d_{3z^2-r^2}$ orbital has the same width as those for the d_{xz} and d_{yz} orbitals. This is reasonable according to

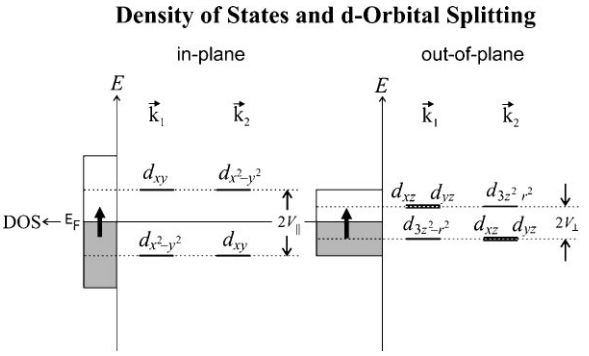

Fig. 12. Schematic model for the density of minority spin states for a free Co monolayer. The half-filled minority band may be separated into contributions from in-plane and out-of-plane d states, as shown. The in-plane bandwidth is larger because of the preferential in-plane bonds between the Co atoms and the empty and filled states have an average separation $2V_{\parallel}$. The narrower band of the out-of-plane d orbitals has an average separation between the empty and filled states of $2V_{\perp}$. The band picture may be represented by a ligand field model where the in-plane and out-of-plane d orbitals are separated by $2V_{\parallel}$ and $2V_{\perp}$, respectively, and an average is performed over two cases ($\boldsymbol{k}_1$ and $\boldsymbol{k}_2$) with the empty and filled d orbitals being exchanged, as shown.

Fig. 10. The band picture may be represented by a ligand field model where the in-plane d_{xy} and $d_{x^2-y^2}$ orbitals are separated by $2V_{\parallel}$ and the out-of-plane d_{xz}, d_{yz}, and $d_{3z^2-r^2}$ orbitals are separated by $2V_{\perp}$, as shown. In order to account for the Brillouin zone averaged densities of states it is then necessary to average over two cases, labelled $\boldsymbol{k}_1$ and $\boldsymbol{k}_2$, where the empty and filled d orbitals are exchanged. The wave vector reflects the fact that the two cases may be thought of as band splittings at two different points $\boldsymbol{k}_1$ and $\boldsymbol{k}_2$ in the Brillouin zone. See for example Fig. 2 in Wang et al. [26], where the order of the band states is inverted at the $\bar{\Gamma}$ and $\bar{M}$ points, respectively.

The model shown in Fig. 12 for a free Co monolayer with $V_{\parallel} > V_{\perp}$ can be generalized to cases with any $V_{\parallel}/V_{\perp}$ ratio. For a sandwich of the form X/Co/X the out-of-plane bandwidth is determined by the overlap of the Co d orbitals with those of the sandwich layers X. Harrison (see chapter 20 in Ref. [95]) has tabulated interaction strengths between different elements. If the in-plane Co–Co bonding strength is normalized to 1.00, then the corresponding out-of-plane Co–X bonding strength is 1.53, 1.60, 1.38, 0.83 for X = Au, Pt, Pd, and Cu, respectively [26]. Hence we would predict that for a Au/Co/Au sandwich the out-of-plane bandwidth is larger than the in-plane one (i.e. $V_{\perp} > V_{\parallel}$), in good accord with the dramatic increase in $d_{3z^2-r^2}$ bandwidth shown in Fig. 11.

4.2.2. Orbital moment and spin–orbit energy anisotropy in ligand field model

By use of the simple ligand field concept we can now calculate the anisotropy of the orbital moment for different bonding situations by use of perturbation theory [11,24,55]. The results for a Co ML corresponding to $V_{\parallel} > V_{\perp}$ are given in Fig. 13. Here we have for simplicity assumed a level splitting corresponding to the center of the BZ for a (1 0 0) monolayer. The in-plane and out-of-plane splittings of the non-perturbed states are

$$2V_{\parallel} = E_{d_{xy}} - E_{d_{x^2-y^2}} \equiv \Delta_{(xy)(x^2-y^2)}, \tag{12}$$

$$2V_{\perp} = E_{d_{yz}} - E_{d_{3z^2-r^2}} \equiv \Delta_{(yz)(3z^2-r^2)}, \tag{13}$$

where $\Delta_{(n)(m)}$ denotes the energy difference between the orbital states d_n and d_m. The results in Fig. 13 are obtained from Eq. (C.5) in Appendix C. We can now apply the results in Fig. 13 to our model shown in Fig. 12 and assuming a half-filled spin-up band and a completely filled spin-down band we obtain using the definition $R = V_{\perp}/V_{\parallel}$,

$$m_o^{\parallel} = \frac{\xi\mu_B}{2V_{\parallel}}\left(\frac{3}{R} + \frac{2}{R+1}\right) \tag{14}$$

and

$$m_o^{\perp} = \frac{\xi\mu_B}{2V_{\parallel}}4. \tag{15}$$

Here ξ is the spin–orbit coupling constant which for Co has a value close to $\xi = 70$ meV [21,84]. Similarly, we obtain from Eqs. (C.6) and (C.8) in Appendix C for the magnetocrystalline anisotropy energy if we neglect spin-flip terms ($\Delta E_{jj'} = 0$),

$$\langle H_{so}^{\parallel}\rangle = -\frac{\xi}{4\mu_B} m_o^{\parallel} \tag{16}$$

and

$$\langle H_{so}^{\perp}\rangle = -\frac{\xi}{4\mu_B} m_o^{\perp}. \tag{17}$$

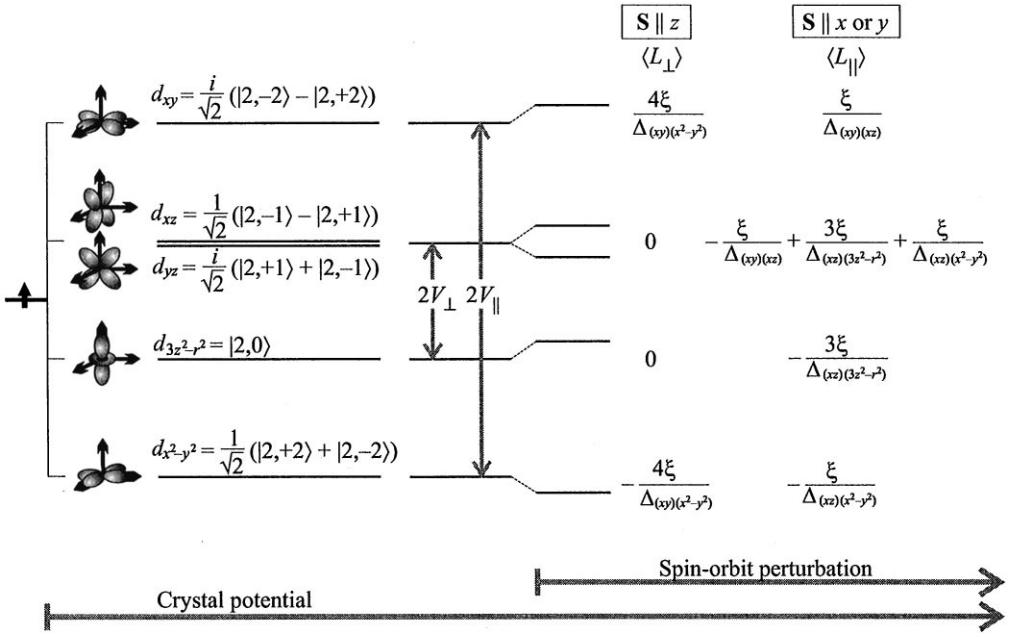

Fig. 13. Orbital momentum in a ligand field model with tetragonal or hexagonal symmetry. For simplicity we assume that the magnetic exchange splitting is large and we consider only states of one spin. Band structure or ligand field effects result in d orbitals which are linear combinations of functions $|l, m_l\rangle$ ($-2 \leqslant m_l \leqslant +2$). We show an energy level scheme corresponding to that at the center of the BZ for a free Co monolayer with cubic (1 0 0) structure [26], where the in-plane splitting ($2V_{\parallel}$) is larger than the out-of-plane splitting ($2V_{\perp}$). The pure d orbitals possess no orbital momentum. The inclusion of the spin–orbit interaction in lowest order perturbation theory results in new states which have anisotropic orbital momenta (units $\hbar$) as shown, where ξ (~ 0.07 eV for Co) is the spin–orbit coupling constant and $\Delta_{(i)(j)} \approx 1$ eV is the energy separation (taken positive) between a higher energy state i and a lower state j. The indicated orbital momenta for spin alignment $\boldsymbol{S}\|z$ and $\boldsymbol{S}\|x$ or y result from mixing of the spin-up states, only. Note that the total orbital momentum (sum) vanishes if all states are empty or full.

We obtain for the MCA energy,

$$\Delta E_{\mathrm{so}} = \frac{\xi}{4\mu_{\mathrm{B}}}(m_{\mathrm{o}}^{\parallel} - m_{\mathrm{o}}^{\perp}) = \frac{\xi^2}{8V_{\parallel}}\left(\frac{3}{R} + \frac{2}{R+1} - 4\right). \tag{18}$$

The anisotropies of the orbital moment m_{o}^{α} and the spin–orbit energy $\langle H_{\mathrm{so}}^{\alpha}\rangle$ as a function of $R = V_{\perp}/V_{\parallel}$ according to Eqs. (14)–(17) are plotted in Fig. 14. We see the preference for an in-plane easy axis for $V_{\parallel} > V_{\perp}$, revealed by the fact $m_{\mathrm{o}}^{\parallel} > m_{\mathrm{o}}^{\perp}$, and for an out-of-plane easy axis for $V_{\perp} > V_{\parallel}$. This result is in good accord with the predictions of the simple model shown in Fig. 9.

Our model also gives quantitative results surprisingly similar to those obtained by means of first principles calculations. From Figs. 10 and 12 we see that for a Co monolayer the in-plane bandwidth is about $4V_{\parallel} \sim 4$ eV and $R = V_{\perp}/V_{\parallel} = 0.5$. Using the values $V_{\parallel} = 1$ eV and $R = V_{\perp}/V_{\parallel} = 0.5$ eV and $\xi = 0.07$ eV/atom we obtain $\Delta E_{\mathrm{so}} = \langle H_{\mathrm{so}}^{\perp}\rangle - \langle H_{\mathrm{so}}^{\parallel}\rangle = 2.0 \times 10^{-3}$ eV/atom, close to the value $\Delta E_{\mathrm{so}} = 1.5 \times 10^{-3}$ eV/atom (using our sign convention) calculated by Daalderop et al. [63] for a free Co monolayer. For a Au/Co/Au sandwich we would also expect $V_{\parallel} = 1$ eV and using Harrison's estimates of the in-plane (Co–Co) versus out-of-plane (Co–Au) bonding strengths we estimate $R = V_{\perp}/V_{\parallel} = 1.5$. With the values $V_{\parallel} = 1$ eV, $R = V_{\perp}/V_{\parallel} = 1.5$ and $\xi = 0.07$ eV/atom we obtain $\Delta E_{\mathrm{so}} = -0.7 \times 10^{-3}$ eV/atom, close to the value $\Delta E_{\mathrm{so}} = -1.0 \times 10^{-3}$ eV/atom (using our sign convention) calculated by Újfalussy et al. [83].

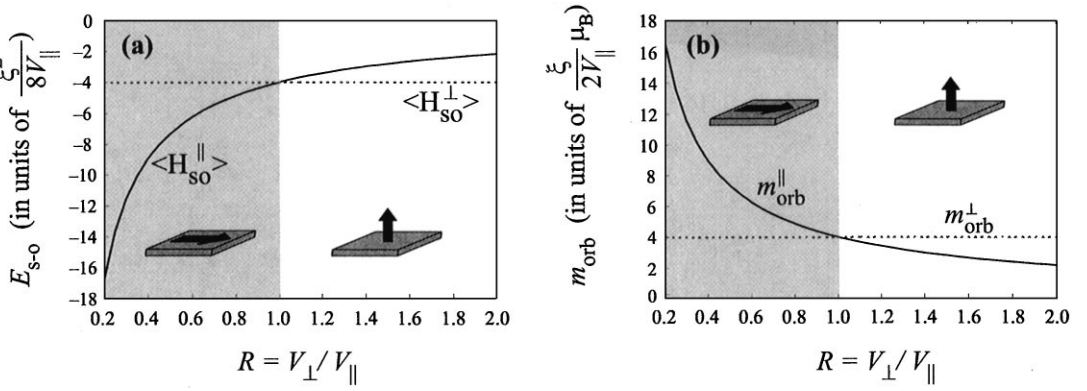

Fig. 14. (a) Spin–orbit energies as a function of $R = V_\perp/V_\parallel$ based on the ligand field model in Fig. 12 with a half-filled minority band (2.5 electrons), for the case when the sample is magnetized in-plane ($\langle H_\parallel \rangle$) and out-of-plane ($\langle H_\perp \rangle$). (b) In-plane and out-of-plane orbital moments as a function of R. The easy magnetization direction lies in-plane for $R < 1$ (shaded region), as indicated by the icons in the plot and out-of-plane for $R > 1$.

Note that the simple picture presented by Fig. 14 does not include the effect of the shape anisotropy which favors an in-plane orientation. The transition from in-plane to out-of-plane easy magnetization is therefore actually shifted to $R > 1$.

4.2.3. Majority band contribution to the orbital moment and the MCA

In the previous Section we focussed on the close correspondence of the orbital moment anisotropy and the spin–orbit energy anisotropy. As shown in Appendix C this correspondence only holds under two key assumptions: (i) that the spin-flip terms involving matrix elements between minority and majority bands are negligibly small and (ii) that the majority (spin-down) band is full. In the following we shall look at the validity of these assumptions.

Let us first consider the size of the spin-flip terms using our ligand field model under the assumption that the majority band is full. The spin–orbit energy anisotropy consists of two terms corresponding to contributions from states with equal spin, ΔE_{jj}, and unequal spin, $\Delta E_{jj'}$, as discussed in Appendix C. We can expand our model shown in Fig. 12 to also include the majority spin-down band, as shown in Fig. 15. We then obtain,

$$\Delta E_{so} = \Delta E_{jj} + \Delta E_{jj'} = \frac{\xi^2}{4\hbar^2}\left(\sum_{n,m}\frac{|\langle d_n^+|L_z|d_m^+\rangle|^2 - |\langle d_n^+|L_x|d_m^+\rangle|^2}{\Delta_{nm}} + \sum_{i,m}\frac{|\langle d_i^-|L_x|d_m^+\rangle|^2 - |\langle d_i^-|L_z|d_m^+\rangle|^2}{\Delta_{im}}\right), \quad (19)$$

where the indices n and m label spin-up filled and empty states, respectively, and i labels spin-down filled states. Note Δ_{im} is negative. We obtain from Eqs. (18) and (19),

$$\Delta E_{so} = \frac{\xi}{4\mu_B}(m_o^{\parallel} - m_o^{\perp}) + \Delta E_{jj'}, \quad (20)$$

indicating that a direct proportionality between the orbital moment anisotropy and the spin–orbit energy anisotropy holds only if the spin-flip term $\Delta E_{jj'}$ is much smaller than the non-spin-flip term $\Delta E_{jj} = \xi(m_o^{\parallel} - m_o^{\perp})/4\mu_B$.

Defining $A = \Delta_{ex}/V_\parallel$ we obtain for the spin-flip term under the condition $\Delta_{ex} > V_\parallel, V_\perp$,

$$\Delta E_{jj'} = \frac{\xi^2}{8V_\parallel}\left(-\frac{1}{A+R-1} + \frac{2}{A} - \frac{1}{A-R+1} - \frac{6}{A+2R} - \frac{2}{A+R+1} + \frac{8}{A+2}\right). \quad (21)$$

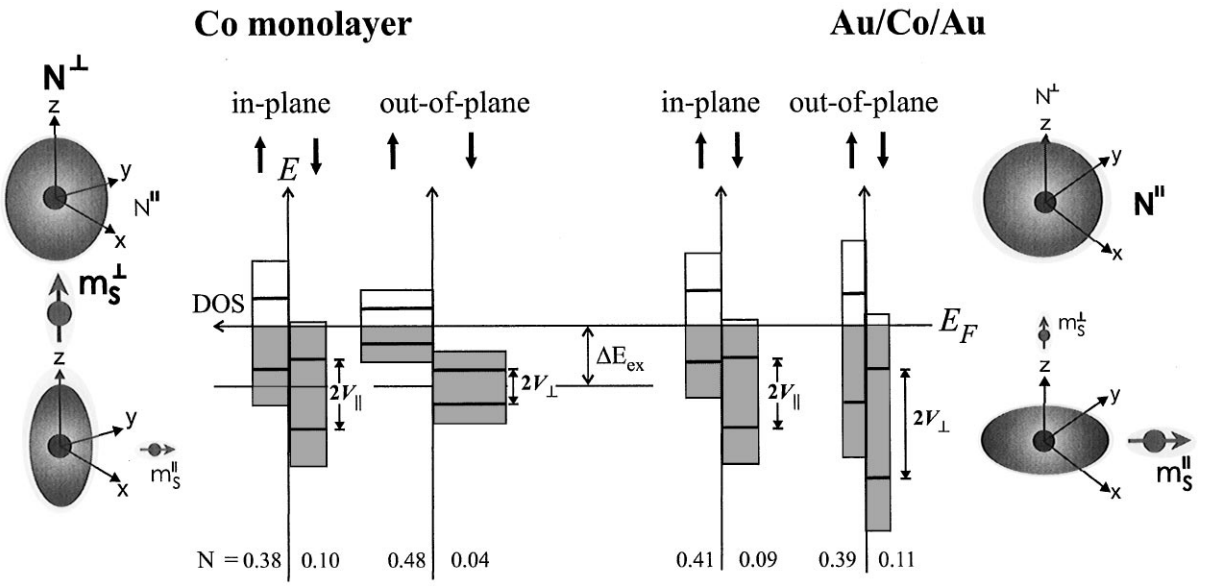

Fig. 15. Schematic density of states (boxes) and ligand field (horizontal energy levels in boxes) models for a free Co monolayer and a Au/Co/Au sandwich, based on bandstructure results [63] and our experimental results, respectively. The Co monolayer model is similar to that shown in Fig. 12 but includes the majority bands. We also list the theoretical (Co monolayer) and experimentally (Au/Co/Au) determined in-plane and out-of-plane spin-dependent number of d holes.

In the limit of large exchange splitting $\Delta_{ex} \gg V_{\parallel}, V_{\perp}$ the various terms in Eq. (21) cancel each other and the spin-flip contribution to the anisotropy vanishes. The other limit is the case $\Delta_{ex} = 0$ ($A = 0$). For $A < 1$ the highest spin-down states (both in- and out-of-plane) in Fig. 15 become unoccupied and no longer contribute to $\Delta E_{jj'}$. We obtain,

$$\Delta E_{jj'} = \frac{\xi^2}{8V_{\parallel}}\left(-\frac{6}{A+2R} - \frac{2}{A+R+1} + \frac{8}{A+2}\right). \tag{22}$$

It is seen by comparison of Eqs. (18) and (22) that the spin-flip contribution always has the opposite sign of the non-spin-flip one and has a smaller magnitude. Hence in Eq. (20) the spin–orbit energy anisotropy is *decreased* relative to that calculated from the orbital moment anisotropy. In the limit $\Delta_{ex} = 0$ ($A = 0$) the non-spin-flip and spin-flip contributions are of equal size and cancel each other, $\Delta E_{jj'} = -\Delta E_{jj}$.

From Figs. 10 and 12 we see that for a Co monolayer the in-plane bandwidth is about $4V_{\parallel} \sim 4$ eV and the exchange splitting is about $\Delta_{ex} \sim 2V_{\parallel} \sim 2$eV. For a Au/Co/Au sandwich we would expect the same values of Δ_{ex} and $V_{\parallel}$ and using Harrison's estimates of the in-plane (Co–Co) versus out-of-plane (Co–Au) bonding strengths we estimate $R = V_{\perp}/V_{\parallel} = 1.5$. With these values we calculate $\Delta E_{jj'}/\Delta E_{jj} = -0.25$ from Eqs. (18) and (21). Hence the spin-flip term is predicted to be much smaller than the non-spin-flip term and the easy axis is therefore determined by ΔE_{jj}, i.e. by the preferred direction of the orbital moment according to Eqs. (16) and (17). Similar conclusions about the size of the spin-flip terms have previously been reached by Wang et al.[5]

[5] Wang et al. [25] have shown that for a filled spin-up band the anisotropy of the spin-flip term $E_{jj'}$ is much smaller than that of the term E_{jj}. This is seen from their expression for $\Delta E_{jj'}$ given by our Eq. (27). This result is derived by replacing the denominator in the spin-flip terms in Eqs. (C.6) or Eq. (19) by the exchange splitting Δ_{ex}, and assuming that it is larger than the crystal potential splitting. The spin-down states are then eliminated by summing over them.

Let us now investigate our second assumption of a filled majority band. Again we shall use our ligand field model in Figs. 12 and 15 for an estimate of effects due to a partially filled majority band and we shall neglect spin-flip terms. We shall assume that the spin-up minority band is half-full (2.5 electrons and holes), as before, and assume that the highest energy majority states are unoccupied. In particular, we shall consider the case $V_\perp > V_\parallel$ appropriate for Au/Co/Au and assume that the highest out-of-plane ligand field state is partly unoccupied with a hole population $0 < w < 1$. According to Eq. (C.5) we can calculate the combined orbital moment due to minority and majority states that would be measured in an XMCD experiment and obtain,

$$m_o^\parallel - m_o^\perp = \frac{\xi\mu_B}{2V_\parallel}\left[\frac{3}{R} + \frac{2}{R+1} - 4 - w\left(\frac{3}{R} + \frac{1}{R+1}\right)\right]. \quad (23)$$

Note that the minority and majority contributions enter with *opposite* sign (see Eq. (C.5)). Alternatively, we can calculate the spin–orbit energy anisotropy according to Eq. (C.7), ignoring all spin-flip terms. Now the minority and majority contributions enter with the *same* sign and we obtain,

$$\Delta E_{so} = \frac{\xi^2}{8V_\parallel}\left[\frac{3}{R} + \frac{2}{R+1} - 4 + w\left(\frac{3}{R} + \frac{1}{R+1}\right)\right]. \quad (24)$$

The spin–orbit energy anisotropy is therefore related to the one calculated from the orbital moment anisotropy $\Delta E_{m_o} = \xi(m_o^\parallel - m_o^\perp)/4\mu_B$ that would be measured by XMCD according to

$$\Delta E_{so} = \Delta E_{m_o} + \Delta E_{fil} \quad (25)$$

with

$$\Delta E_{fil} = \frac{w\xi^2}{4V_\parallel}\left[\frac{3}{R} + \frac{1}{R+1}\right]. \quad (26)$$

Since the first term in Eq. (25) is negative for $V_\perp > V_\parallel$, the second, positive, term ΔE_{fil} *decreases* the spin–orbit energy anisotropy over the value calculated from the orbital moment anisotropy, similar to the term $\Delta E_{jj'}$ in Eq. (20).

For $R = V_\perp/V_\parallel = 1.5$ we obtain $\Delta E_{fil}/\Delta E_{m_o} = -4w/(1+2w)$. This is a strongly varying function of w but for a realistic value of $w = 0.1$ we obtain $\Delta E_{fil}/\Delta E_{m_o} = -\frac{1}{3}$ indicating again that the spin–orbit energy anisotropy is dominated by the orbital moment anisotropy of the minority band.

5. XMCD results and theoretical models

5.1. Anisotropy of charge and spin density

Our experimental results for Au/Co/Au in Fig. 6c show that the number of 3d holes per atoms is isotropic ($N^\perp = N^\parallel$) within experimental error. The Co charge density in the atomic volume is therefore predicted to be nearly spherical. In contrast, the experimental results in Fig. 8 reveal a significant anisotropy in the spin density m_D^z. At the thin end of the wedge (3 ML Co) we obtain $m_s = 1.43\ \mu_B$, $m_D^\perp = 0.15\ \mu_B$ and $m_D^\parallel = -0.075\ \mu_B$ from Fig. 8 which yields $m_s^\perp = 0.27\ \mu_B$ and $m_s^\parallel = 0.31\ \mu_B$ according to Eq. (6). In 3d metals the anisotropy in the spin density is mainly induced by the bonding anisotropy, i.e. by the anisotropic charge distribution in the unit cell because of the small spin–orbit coupling. If the majority band is completely full the charge and spin distributions are identical. Our results therefore reveal that the majority band is not completely filled. Combining our charge and spin results we can obtain the in-plane and out-of-plane number of majority and minority holes. Using the experimental values for 3 ML Co thickness $N^\parallel = N_\uparrow^\parallel + N_\downarrow^\parallel = N^\perp = N_\uparrow^\perp + N_\downarrow^\perp = 2.5/5 = 0.50$ and $m_s^\parallel = (N_\uparrow^\parallel - N_\downarrow^\parallel)\,\mu_B = 0.31\ \mu_B$ and $m_s^\perp = (N_\uparrow^\perp - N_\downarrow^\perp)\,\mu_B = 0.27\ \mu_B$ we obtain $N_\uparrow^\parallel = 0.41$, $N_\downarrow^\parallel = 0.09$, $N_\uparrow^\perp = 0.39$ and $N_\downarrow^\perp = 0.11$. The results are graphically illustrated in Fig. 15 together with those for a free Co monolayer as calculated by Daalderop [63]. The various anisotropies for Au/Co/Au are found to be opposite to those for a free Co monolayer, in support of the discussion in Section 4.2.1.

Our finding of a significant number of majority holes has implications for the contribution of the majority band to the orbital moment and spin–orbit energy anisotropies as discussed in Section 4.2.3. The holes in the majority band give rise to

a term $\Delta E_{\rm fil}$ (Eq. (26)) and cause a break down of the simple proportionality of the spin–orbit energy anisotropy with the orbital moment anisotropy according to Eq. (25). This will be discussed in more detail in Section 5.2 below.

There is also an interesting connection of the charge and spin density anisotropies with the spin-flip terms discussed in Section 4.2.3. Wang et al. [25] (see footnote 5), showed that in the limit of large exchange splitting and a filled majority band the quadrupolar charge density, which in this model is identical to the spin density, gives rise to a magnetic anisotropy contribution which is proportional to the spin-flip term $\Delta E_{jj'}$ discussed in Section 4.2.3. Using our notation the result of Wang et al. is given by (see footenote 5)

$$\Delta E_{jj'} = \frac{-\xi^2}{8\hbar^2 \Delta_{\rm ex}} \sum_{n,k,E} \langle \phi_n^+(\boldsymbol{k}, E)|3L_z^2 - L^2|\phi_n^+(\boldsymbol{k}, E)\rangle$$
$$= \frac{-\xi^2}{8\hbar^2} \frac{\langle Q_{zz}^{\rm L}\rangle}{\Delta_{\rm ex}} = \frac{-21\xi^2}{16} \frac{\langle Q_{zz}\rangle}{\Delta_{\rm ex}}. \quad (27)$$

In this case the anisotropy depends only on the quadrupole moment (see Appendix A) of the occupied states in the spin-up minority band and is inversely proportional to the exchange splitting (note that the filled subband has $\langle Q_{zz}^{\rm L}\rangle = 0$). In this model our result of a vanishing small white line anisotropy for Au/Co/Au for all Co thicknesses, i.e. $N_{\rm Q}^{\alpha} = 7/8\langle Q_{\alpha\alpha}\rangle \sim 0$, would predict a negligibly small contribution to the magnetic anisotropy due to the quadrupolar charge (= spin) anisotropy.

The result of Wang et al. was extended by Dürr and van der Laan [42,85] to the general case of minority as well as majority spin contributions, the situation encountered for our Au/Co/Au structure. It was proposed that, in general, the intra-atomic magnetic dipole term plays a role for the MCA through a term $\boldsymbol{S}\cdot\boldsymbol{T}$ that couples the atomic spin with the dipole operator. Since for transition metals the dipole operator is approximately given by $T_\alpha = (2/21\hbar^2)(3L_\alpha^2 - L^2)S_{\tilde{z}}$ (see Appendices A and B), a magnetic anisotropy results from the spin–orbit coupling, and the $\boldsymbol{S}\cdot\boldsymbol{T}$ term is related to the spin-flip anisotropy energy $\Delta E_{jj'}$ discussed in Section 4.2.3. Estimates of the spin-flip anisotropy energy from our measured anisotropy of the dipole moments $m_{\rm D}^{\alpha} = -7\langle T_\alpha\rangle\mu_{\rm B}/\hbar$ (see Fig. 8) again predict a small spin-flip contribution to the spin–orbit anisotropy.

The contribution of the intra-atomic dipole moment to the magnetic anisotropy suggested by Wang et al. and by Dürr and van der Laan is based on spin–orbit coupling. Since for 3d metals the intra-atomic magnetic dipole term is mainly determined by the anisotropy of the lattice there is also a magnetostatic contribution to the magnetic anisotropy, as discussed in Section 4.1. This is due to a quadrupole term in the magnetostatic energy. We may estimate the size of this anisotropy energy from the Au/Co/Au data at a Co thickness of 3 ML (Fig. 8). We use the experimentally determined quadrupole term in the spin density $m_{\rm D}^{\perp}/2 = m_{\rm D}^{\parallel} = 0.075\ \mu_{\rm B}$ and the spin moment $m_{\rm s} = 1.5\ \mu_{\rm B}$ to estimate the size of the quadrupole induced magnetostatic anisotropy relative to the monopole term to be $m_{\rm D}^{\perp}/2m_{\rm s} = 0.05$ (see footnote 3). Hence we conclude that, in practice, the intra-atomic magnetic dipole moment plays a negligible role for the magnetic anisotropy.

5.2. Anisotropy of orbital moment

The anisotropy of the orbital moment shown in Fig. 7c qualitatively shows the same thickness dependence as the energy anisotropy shown in Fig. 4c obtained from the Kerr measurements. We can use the XMCD values for $m_{\rm o}^{\perp} - m_{\rm o}^{\parallel}$ to calculate the corresponding spin–orbit energy anisotropy by use of the spin–orbit coupling constant for Co which we assume to have the value $\xi = 70$ meV [21,84]. Because of the problems associated with extrapolations we shall simply compare the XMCD and Kerr results obtained at a Co thickness of 3 ML. The XMCD value $m_{\rm o}^{\perp} - m_{\rm o}^{\parallel} = (0.22 \pm 0.05)\ \mu_{\rm B}$/atom then yields the anisotropy energy $\Delta E_{\rm so} = \xi(m_{\rm o}^{\parallel} - m_{\rm o}^{\perp})/4 = -3.8 \times 10^{-3}$ eV/atom. Here we have used Eq. (18), i.e. neglected the spin-flip terms $\Delta E_{jj'}$ in Eq. (20) and assumed a filled majority band so that the term $\Delta E_{\rm fil}$ in Eq. (25) is negligible. This value is larger than the Kerr result $\Delta E_{\rm so} = -2.55\ {\rm MJ/m^3} = -1.8 \times 10^{-4}$ eV/atom (Fig. 4c) by a factor of about 20.

The anisotropy energy calculated from the orbital moment anisotropy using the proportionality factor $C = \xi/4$ (see Eqs. (11) and (18)) obtained by

perturbation theory is therefore significantly in error. Comparing experimental Kerr and XMCD values for 3 ML Co we obtain the proportionality factor C in Eq. (11) to be $C = 0.8 \times 10^{-3}$ eV/μ_B which is the same as that obtained for Co/Pd multilayers by Dürr et al [86]. A similar value, $C = 0.68 \times 10^{-3}$ eV/μ_B, has recently been obtained from ferromagnetic resonance data for the BCC $Fe_2/V_5(0\,0\,1)$ superlattice system [87]. On the theory side larger C values have been obtained that are in closer agreement with the perturbation value $\xi/4 = 1.8 \times 10^{-2}$ eV/μ_B. Using a fully relativistic spin polarized theory for Au(1 1 1)/Co(1 ML)/Au(∞), Újfalussy et al. [83] obtained $C = 5 \times 10^{-2}$ eV/μ_B. Dürr et al. [37] obtained 1.6×10^{-2} eV/μ_B from electronic structure calculations for face centered tetragonal (FCT) Ni and Co and Hjortstam et al. [88] obtained approximately 2.6×10^{-2} eV/μ_B for FCT Ni, although the relationship between ΔE_{so} and Δm_o was found to be only approximately linear as a function of the FCT c/a ratio.

The reason for the discrepancy between the MCA energy calculated from the XMCD orbital moment anisotropy and that obtained from Kerr measurements remains to be explained. A possible source for the discrepancy is the majority band contribution discussed in Section 4.2.3. Eqs. (20) and (25) may be written in the general form $\Delta E_{so} = \Delta E_{m_o}[1 + \Delta E_{maj}/\Delta E_{min}]$ where the term ΔE_{maj} represents either the spin-flip or the direct majority band contribution. In order to obtain the Kerr value $\Delta E_{so} = -1.8 \times 10^{-4}$ eV/atom for 3 ML Co in Au/Co/Au the XMCD value $\Delta E_{m_o} = -3.8 \times 10^{-3}$ eV/atom needs to be corrected by $[1 + \Delta E_{maj}/\Delta E_{min}] = 0.05$. This would require an almost equal contribution $\Delta E_{maj} = -0.95\Delta E_{min}$ of the majority and minority bands to the spin–orbit anisotropy. Our estimates in Section 4.2.3 and Section 5.1 of the majority band contributions to the MCA, yielding $|\Delta E_{maj}/\Delta E_{min}| < 0.4$, make it very unlikely that the discrepancy can be entirely explained by either the spin-flip terms or by incomplete filling of the majority band.

A possible explanation is provided by the fact that XMCD is a local, element specific, probe. In our case the determined orbital moments are those of the Co atoms alone. In contrast, the total MCA and the Kerr measurements contain contributions from magnetically polarized Au atoms at the interfaces. Interfacial hybridization between Co and Cu states in Co/Co multilayers has been observed experimentally and theoretically [89] and it is responsible for an appreciable magnetic moment on Cu interface atoms [31]. Similar effects are expected for Co/Au sandwiches. As revealed by Figs. 11 and 15 the hybridization of Co and Au atoms at the interface leads to an increase in bandwidth. The Co derived minority d states, which are mostly responsible for the orbital moment, are concentrated in the region -3 to $+1$ eV relative to the Fermi level (see Fig. 10) while the Au d states lie in the -7.5 to -2 eV range [90]. According to Eq. (18) the MCA energy and orbital moment anisotropy are inversely proportional to the average separation ($V_\parallel$ or $V_\perp$) between the filled and empty minority states. If all Co–Au hybridized states are considered the effective V is considerably larger than for the Co states only. The reduced moment associated with the Au derived states may be offset by the larger size of the spin–orbit coupling constant ($\xi_{Au}/\xi_{Co} \sim 7$) [91]. Qualitatively, one would therefore expect the MCA determined by XMCD (Co states only) to be significantly larger than that obtained by Kerr measurements (Co–Au states). Clearly, more theoretical and experimental work is needed to explore the quantitative correlation between the orbital moment anisotropy measured by XMCD and the true spin–orbit energy anisotropy.

Despite the quantitative discrepancy of the XMCD and Kerr results the orbital moment anisotropy obtained from XMCD provides experimental verification of a simple picture for the microscopic origin of the MCA shown in Fig. 9. At the thick end of the wedge the orbital magnetic moment is nearly isotropic. Here, the overall in-plane anisotropy of the sample is simply due to the macroscopic shape anisotropy. With decreasing sample thickness, the average symmetry of the Co atoms becomes increasingly anisotropic. At the thin end of the wedge the anisotropy of the orbital moment has become so large that it has a strong preference for a perpendicular orientation. Now there are two opposing forces acting on the spin moment. The dipolar field wants to rotate it in-plane and the spin–orbit coupling wants to rotate it

parallel to the out-of-plane orbital moment (Hund's third rule). The easy axis is determined by which of the two forces is stronger, i.e. whether the dipolar energy is smaller or larger than the anisotropy of the spin–orbit energy. Clearly, at the thin edge of the wedge the anisotropy energy associated with the spin–orbit interaction exceeds the value of the shape anisotropy and we have the interesting situation that the small orbital moment redirects the larger spin moment into a perpendicular alignment.

6. Summary and conclusions

The present paper discusses the use of XMCD spectroscopy to explore the microscopic origin of electronic and magnetic anisotropies in transition metal thin films, in particular, for Co in a Au/Co-staircase/Au sample. XMCD spectroscopy is shown to provide detailed information on the anisotropy of the atomic charge and spin in the atomic cell. For thin films with uniaxial anisotropy around the surface normal, angle-dependent XMCD measurements in strong magnetic fields are shown to quantitatively determine the in-plane and out-of-plane spin-dependent d-band occupations. These results complement those obtained from first principles electronic structure calculations.

The anisotropy of the orbital magnetic moment is shown to be especially important because of its close link to the magnetocrystalline anisotropy. A simple picture based on anisotropic bonding is developed that allows one to visualize the preferred direction of the orbital moment. The picture is based on the well-known textbook concept of orbital moment quenching by a ligand field. The connection is made between this simple picture and the concepts and results of electronic structure calculations. Model calculations that link ligand field and band structure concepts are carried out to explore the link between orbital moment anisotropy and spin–orbit energy anisotropy. They are found to have remarkably predictive capabilities.

XMCD results for Au/Co/Au are discussed in terms of the presented theoretical model. Our results lead to a particularly illustrative picture for the origin of the magnetocrystalline anisotropy based on the preferred direction of the orbital moment.

Acknowledgements

This work was carried out in part at SSRL which is operated by the Department of Energy, Division of Chemical Sciences. I would like to thank my collaborators who were involved in the original work reviewed here, especially Dieter Weller, Reiko Nakajima, Mahesh Samant, and Claude Chappert. I am also indebted to Balazs Ujfalussy for providing unpublished theoretical results for Au/Co/Au, to Olle Eriksson for elucidating discussions about orbital polarization and hybridization effects, and to Patrick Bruno for pointing out references to early work on orbital anisotropy.

Appendix A. Charge density term and quadrupole operator

The terms N and N_Q^α in the charge sum rule reflect the monopole and quadrupole contributions of the charge distribution in the atomic sphere. N_Q^α can be expressed in terms of the quadrupole operator of the charge, $Q_{\alpha\beta} = \delta_{\alpha\beta} - 3\hat{r}_\alpha\hat{r}_\beta$. $Q_{\alpha\beta}$ is a second rank tensor with the symmetry properties $Q_{\alpha\beta} = Q_{\beta\alpha}$ and $\sum_\alpha Q_{\alpha\alpha} = 0$. The tensor elements $Q_{\alpha\beta}$ can be expressed as a linear combination of the well-known spherical harmonics $Y_l^m(\theta, \phi)$ with $l = 2$ and $-2 \leqslant m \leqslant 2$. For example, the quadrupole moment of the charge is given by $\langle Q_{zz}\rangle = \langle 1 - 3\cos^2\theta\rangle = -\sqrt{16\pi/5}\langle Y_2^0\rangle$ and it is related to the quadrupole moment of the angular momentum $\langle Q_{zz}^L\rangle = \langle 3L_z^2 - L^2\rangle = (21\hbar^2/2)\langle Q_{zz}\rangle$.

Let $\phi_n(\boldsymbol{k}, E) = \sum_{i,j} a_{i,n}^j(\boldsymbol{k}, E) d_i \chi^j$ denote a band state with spin functions $\chi^j (j = \pm)$. We then obtain $\langle Q_{\alpha\alpha}\rangle = \sum_{n,k,E}\langle\phi_n(\boldsymbol{k}, E)|Q_{\alpha\alpha}|\phi_n(\boldsymbol{k}, E)\rangle = \sum_i \langle d_i|Q_{\alpha\alpha}|d_i\rangle \sum_{n,k,E,j}|a_{i,n}^j(\boldsymbol{k}, E)|^2$. The last sum is just the d orbital projected number of electrons (or holes) $N^i = \sum_{n,k,E,j}|a_{i,n}^j(\boldsymbol{k}, E)|^2$ and the matrix elements $Q_\alpha^i = \langle d_i|Q_{\alpha\alpha}|d_i\rangle$ have been tabulated by Stöhr and König [34]. This gives $N_Q^\alpha = (7/B)\sum_i Q_\alpha^i N^i = (7/B)\langle Q_{\alpha\alpha}\rangle$. Here $B = -4$ for

linearly polarized light (electric field vector $\boldsymbol{E}\|\alpha$), and $B = 8$ for circularly or plane polarized light (X-ray wave vector $\boldsymbol{k}\|\alpha, \boldsymbol{E}\perp\boldsymbol{k}$) [41]. Note that the quantities $N_{\mathrm{Q}}^{\alpha} = (7/4)\langle Q_{\alpha}^{i}\rangle$ ($\alpha = x, y, z$) correspond to the diagonal components of a normalized quadrupole tensor of the charge (holes), also called orientation matrix or Saupe matrix [92] and they are identical to the quadrupole terms in the multipole expansion of the charge [93].

Appendix B. Spin density term and magnetic dipole operator

The terms m_{s} and m_{D}^{α} in the spin sum rule reflect the monopole and quadrupole contributions of the spin distribution in the atomic sphere. In general, m_{D}^{α} is defined as the expectation value of the intra-atomic magnetic dipole operator $\boldsymbol{T} = \boldsymbol{S} - 3\hat{\boldsymbol{r}}(\hat{\boldsymbol{r}}\cdot\boldsymbol{S})$, generated by the valence electrons [39], according to Ref. [55] $m_{\mathrm{D}}^{\alpha} = -7\langle T_{\alpha}\rangle\mu_{\mathrm{B}}/\hbar$. In general, one can write $T_{\alpha} = \sum_{\beta} Q_{\alpha\beta}S_{\beta}$, indicating the coupled charge ($\boldsymbol{Q}$) and spin ($\boldsymbol{S}$) components of $\boldsymbol{T}$. Since the quadrupole operator of the charge is related to the quadrupole operator of the angular momentum, as discussed in Appendix A, T_{α} may also be written as a coupled operator involving the spin and the square of the angular momentum.

If we choose the spin quantization axis $\tilde{z}$ along the magnetization direction then the components (S_x, S_y, S_z) of the spin $\boldsymbol{S}$ in the crystal frame are related to the components $(S_{\tilde{x}}, S_{\tilde{y}}, S_{\tilde{x}})$ in the rotated spin frame $(\tilde{x}, \tilde{y}, \tilde{z})$ by $S_x = S_{\tilde{x}}\cos\tilde{\phi}\cos\tilde{\theta} - S_{\tilde{y}}\sin\tilde{\phi} + S_{\tilde{z}}\cos\tilde{\phi}\sin\tilde{\theta}$, $S_y = S_{\tilde{x}}\sin\tilde{\phi}\cos\tilde{\theta} + S_{\tilde{y}}\cos\tilde{\phi} + S_{\tilde{z}}\sin\tilde{\phi}\sin\tilde{\theta}$, and $S_z = -S_{\tilde{x}}\sin\tilde{\theta} + S_{\tilde{z}}\cos\tilde{\theta}$ and the magnetic dipole operator takes the following form for $\boldsymbol{k}, \boldsymbol{H}_{\mathrm{ext}}\|x$, y or z

$$\boldsymbol{k}, \boldsymbol{H}_{\mathrm{ext}}\|x: \quad T_x = Q_{xx}S_{\tilde{z}} + Q_{xy}S_{\tilde{y}} - Q_{xz}S_{\tilde{x}}, \tag{B.1}$$

$$\boldsymbol{k}, \mathrm{H}_{\mathrm{ext}}\|y: \quad T_y = -Q_{yx}S_{\tilde{y}} + Q_{yy}S_{\tilde{z}} - Q_{yz}S_{\tilde{x}}, \tag{B.2}$$

$$\boldsymbol{k}, \boldsymbol{H}_{\mathrm{ext}}\|z: \quad T_z = Q_{zx}S_{\tilde{x}} + Q_{zy}S_{\tilde{y}} + Q_{zz}S_{\tilde{z}}. \tag{B.3}$$

For the 3d transition metals the spin–orbit interaction is much smaller than the exchange interaction and the crystal potential. In this case the expectation values of T_{α} are only slightly affected when spin–orbit perturbed band states are used instead of band states without inclusion of the spin–orbit interaction. That means we can neglect the effect of spin–orbit coupling in evaluating the matrix elements in Eqs. (B.1)–(B.3) and hence all terms containing the spin-flip operators $S_{\tilde{x}}$ and $S_{\tilde{y}}$ do not contribute. We can therefore replace the general operator $T_{\alpha} = \sum_{\beta} Q_{\alpha\beta}S_{\beta}$ simply by $T_{\alpha} = Q_{\alpha\alpha}S_{\tilde{z}}$. Let $\phi_n(\boldsymbol{k}, E) = \sum_{i,j} a_{i,n}^{j}(\boldsymbol{k}, E)d_i\chi^j$ denote a band state with spin functions χ^j ($j = \pm$). We then obtain[6] $\langle T_{\alpha}\rangle = \sum_{n,\boldsymbol{k},E}\langle\phi_n(\boldsymbol{k}, E)|Q_{\alpha\alpha}S_{\tilde{z}}|\phi_n(\boldsymbol{k}, E)\rangle = \sum_i\langle d_i|Q_{\alpha\alpha}|d_i\rangle\sum_{n,\boldsymbol{k},E,j}|a_{i,n}^{j}(\boldsymbol{k}, E)|^2\langle\chi^j|S_{\tilde{z}}|\chi^j\rangle$. The last sum contains just the d orbital projected spin momenta $\langle S_{\tilde{z}}^{i}\rangle = -(\hbar/2\mu_{\mathrm{B}})\sum_i m_{\mathrm{s}}^{i}$ so that we obtain $\langle T_{\alpha}\rangle = -(\hbar/2\mu_{\mathrm{B}})\sum_i Q_{\alpha}^{i}m_{\mathrm{s}}^{i}$, reflecting the decoupled nature of charge and spin. This gives $m_{\mathrm{D}}^{\alpha} = (7/2)\sum_i Q_{\alpha}^{i}m_{\mathrm{s}}^{i}$ which leads to Eq. (6).

There is a formal relationship between the *intra*-atomic dipole moment $\boldsymbol{T} = \sum_j \hat{\boldsymbol{s}}_j - 3\hat{\boldsymbol{r}}_j(\hat{\boldsymbol{r}}_j\cdot\hat{\mathbf{s}}_j)$ generated by the valence electrons, and the *inter*-atomic dipole field $\boldsymbol{H} = (m\mu_0/4\pi)\sum_j(\hat{\boldsymbol{S}}_j - 3\hat{\boldsymbol{r}}_j(\hat{\boldsymbol{r}}_j\cdot\hat{\boldsymbol{S}}_j))/r_j^3$ created at a given atomic site (placed at the origin) by all other moments $m\hat{\boldsymbol{S}}_j$ in the sample at positions $r_j\hat{\boldsymbol{r}}_j$. In particular, the magnetic dipole–dipole interaction given by Eq. (8) can be viewed as the energy of a dipole moment $m\hat{\boldsymbol{S}}$ at the origin in the field of all the other dipoles, according to $E_{\mathrm{dip-dip}} = m\hat{\boldsymbol{S}}\cdot\boldsymbol{H}$. The *intra*-atomic dipole moment $\boldsymbol{T}$ contributes to the magnetic anisotropy in higher order through a quadrupole term (see footnote 3) in the magnetostatic dipole–dipole interaction as discussed in Section 4.1. The quantities $m_{\mathrm{D}}^{\alpha}/2$ correspond to the quadrupole terms in the multipole expansion of the magnetic moment in the unit cell [93] (see footnote 3).

Appendix C. The spin–orbit interaction

Here we briefly discuss the calculation of matrix elements of the anisotropic spin–orbit interaction and the orbital moment using perturbation theory.

[6] For higher than $D_{2\mathrm{h}}$ symmetry all cross terms $\langle d_i|Q_{\alpha\alpha}|d_j\rangle$ in the crystal wave functions vanish. This holds even in the presence of s–o coupling since it does not mix the two $\mathrm{e_g}$ orbitals which give rise to a cross term.

The spin–orbit (s–o) interaction within the d shell

$$H_{so} = \xi \boldsymbol{L}\cdot\boldsymbol{S} = \xi(L_x S_x + L_y S_y + L_z S_z), \tag{C.1}$$

has the effect of mixing different d orbitals and the spin-up and spin-down states. If we choose the spin quantization axis $\tilde{z}$ along the magnetization direction then the components (S_x, S_y, S_z) of the spin $\boldsymbol{S}$ in the crystal frame can be expressed in terms of the components $(S_{\tilde{x}}, S_{\tilde{y}}, S_{\tilde{z}})$ in the rotated spin frame $(\tilde{x}, \tilde{y}, \tilde{z})$ as discussed in Appendix B. This gives the following expressions for $\boldsymbol{H}_{ext}, \tilde{z} \| x, y$ or z

$$\boldsymbol{H}_{ext}\|x: \quad H^x_{so} = \xi(L_x S_{\tilde{z}} + L_y S_{\tilde{y}} - L_z S_{\tilde{x}}), \tag{C.2}$$

$$\boldsymbol{H}_{ext}\|y: \quad H^y_{so} = \xi(-L_x S_{\tilde{y}} + L_y S_{\tilde{z}} - L_z S_{\tilde{x}}), \tag{C.3}$$

$$\boldsymbol{H}_{ext}\|z: \quad H^z_{so} = \xi(L_x S_{\tilde{x}} + L_y S_{\tilde{y}} + L_z S_{\tilde{z}}). \tag{C.4}$$

The angle-dependent orbital moment $m^\alpha_o = -\langle L_\alpha\rangle \mu_B/\hbar$ is calculated by use of the second-order perturbation theory expression [11]

$$\begin{aligned}\langle L_\alpha\rangle &= \frac{2\xi}{\hbar^2}\sum_{k,n,m,j}\frac{|\langle \phi^j_n(\boldsymbol{k})|L_\alpha|\phi^j_m(\boldsymbol{k})\rangle|^2}{\Delta_{nm}}\langle\chi^j|S_{\tilde{z}}|\chi^j\rangle \\ &= \langle L^+_\alpha\rangle - \langle L^-_\alpha\rangle,\end{aligned} \tag{C.5}$$

where the sum extends over filled states n and empty states m within the spin-up and spin-down manifolds (index j) and $\phi^j_n(\boldsymbol{k})$ denotes a zeroth-order band state associated with spin function χ^j, where $\langle\chi^\pm|S_{\tilde{z}}|\chi^\pm\rangle = \pm 1/2$. Matrix elements $\langle d_n|L_\alpha|d_m\rangle$ are given by Ballhausen (see p. 70 in Ref. [96]). Note that the coupling between filled pairs of states or empty pairs of states does not need to be considered since the spin–orbit induced terms cancel each other for any pair. Also, to first-order m^α_o does not depend on the mixing of spin-up and spin-down states by the spin–orbit interaction, since the relevant matrix elements $\langle d_n\chi^+|L_\alpha|d_m\chi^-\rangle = 0$. Thus there are no spin-flip contributions to the orbital moment. According to Eq. (C.5) the orbital momentum is the sum of contributions from all filled states in the spin-up and spin-down subbands. If a subband is filled its contribution vanishes.

The angle-dependent spin–orbit energy is given by the second-order expression

$$\begin{aligned}\langle H^\alpha_{so}\rangle = &\frac{\xi^2}{4\hbar^2}\sum_{k,n,m,j}\frac{|\langle\phi^j_n(\boldsymbol{k})|L_\alpha|\phi^j_m(\boldsymbol{k})\rangle|^2}{\Delta_{nm}} \\ &+ \sum_{k,n,l,j,j'}\frac{|\langle\phi^j_n(\boldsymbol{k})|H^\alpha_{so}|\phi^{j'}_l(\boldsymbol{k})\rangle|^2}{\Delta_{nl}} = E^\alpha_{jj} + E^\alpha_{jj'},\end{aligned} \tag{C.6}$$

where the terms E^α_{jj} and $E^\alpha_{jj'}$ represent the contributions from states of the same and opposite spin, respectively, and the sums extend over filled states (n, j) and empty states (m, j) and (l, j').

It is seen that for $E^\alpha_{jj'} = 0$ we obtain

$$\langle H^\alpha_{so}\rangle = E^\alpha_{jj} = \frac{\xi}{4\hbar}(\langle L^+_\alpha\rangle + \langle L^-_\alpha\rangle), \tag{C.7}$$

showing the direct correlation between the orbital moments of the spin-up and spin-down manifolds and the spin–orbit energy. Note that the contributions of the spin-down states, $\langle L^-_\alpha\rangle$, enter with opposite signs in the expressions for the orbital moment (Eq. (C.5)) and the spin–orbit energy (Eq. (C.7)). In general, we therefore obtain a direct proportionality between the orbital moment and the spin–orbit energy only if $\langle L^-_\alpha\rangle = 0$, i.e. if the spin-down band is full. In the limit of a vanishing exchange splitting the orbital moment vanishes ($\langle L^+_\alpha\rangle = \langle L^-_\alpha\rangle$), and so does the spin–orbit energy ($E^\alpha_{jj} = -E^\alpha_{jj'}$).

With the sign convention of Eq. (11) and footnote 4 the magnetocrystalline anisotropy energy is given by

$$\Delta E_{so} = \langle H^z_{so}\rangle - \langle H^x_{so}\rangle = \langle H^\perp_{so}\rangle - \langle H^\parallel_{so}\rangle. \tag{C.8}$$

References

[1] A.J. Freeman, R. Wu, J. Magn. Magn. Mater. 100 (1991) 497.
[2] O. Eriksson et al., Solid State Commun. 78 (1991) 801.
[3] O. Eriksson et al., Phys. Rev. B 45 (1992) 2868.
[4] Y. Wu, J. Stöhr, B.D. Hermsmeier, M.G. Samant, D. Weller, Phys. Rev. Lett. 69 (1992) 2307.
[5] R. Wu, D. Wang, A.J. Freeman, Phys. Rev. Lett. 71 (1993) 3581.
[6] R. Wu, A.J. Freeman, Phys. Rev. Lett. 73 (1994) 1994.
[7] D. Weller, Y. Wu, J. Stöhr, M.G. Samant, B.D. Hermsmeier, C. Chappert, Phys. Rev. B 49 (1994) 12888.

[8] M. Tischer, O. Hjortstam, D. Arvanitis, J.H. Dunn, F. May, K. Baberschke, J. Trygg, J.M. Wills, B. Johansson, O. Eriksson, Phys. Rev. Lett. 75 (1995) 1602.
[9] N. Nakajima, T. Koide, T. Shidara, H. Miyauchi, H. Fakutani, A. Fujimori, K. Iio, T. Katayama, M. Nývlt, Y. Suzuki, Phys. Rev. Lett. 81 (1998) 5229.
[10] H.A. Dürr, S.S. Dhesi, E. Dudzik, D. Knabben, G. van der Laan, J.B. Goedkoop, F.U. Hillebrecht, Phys. Rev. B 59 (1999) R701.
[11] P. Bruno, Phys. Rev. B 39 (1989) 865.
[12] U. Gradmann, J. Müller, Phys. Stat. Sol. 27 (1968) 313.
[13] U. Gradmann, Appl. Phys. 3 (1974) 161.
[14] F.J.A. den Broeder, W. Hoving, P.J.H. Bloemen, J. Magn. Magn. Mater. 93 (1991) 562.
[15] G.H.O. Daalderop, P.J. Kelly, M.F.H. Schuurmans, Phys. Rev. Lett. 68 (1992) 682.
[16] K. Baberschke, Appl. Phys. A 62 (1996) 417.
[17] B.M. Lairson, M.R. Visokay, R. Sinclair, B.M. Clemens, Appl. Phys. Lett. 62 (1993) 639.
[18] B. Zhang, W.A. Soffa, Scripta Metall. Mater. 30 (1994) 683.
[19] A. Cebollada, D. Weller, J. Sticht, G.R. Harp, R.F.C. Farrow, R.F. Marks, R. Savoy, J.C. Scott, Phys. Rev. B 50 (1994) 3419.
[20] T. Klemmer, D. Hoydick, H. Okumura, B. Zhang, W.A. Soffa, Scripta Metall. Mater. 33 (1995) 1793.
[21] G.H.O. Daalderop, P.J. Kelly, M.F.H. Schuurmans, Phys. Rev. B 41 (1990) 11919.
[22] J. Trygg, B. Johansson, O. Eriksson, J.M. Wills, Phys. Rev. Lett. 75 (1995) 2871.
[23] J.H. Van Vleck, Phys. Rev. 52 (1937) 1178.
[24] P. Bruno, in: Magnetismus von Festkörpern und Grenzflächen, KFA Jülich, Jülich, 1993, p. 24.1.
[25] D. Wang, R. Wu, A.J. Freeman, Phys. Rev. B 47 (1993) 14932.
[26] D. Wang, R. Wu, A.J. Freeman, J. Magn. Magn. Mater. 129 (1994) 237.
[27] G. Schütz, W. Wagner, W. Wilhelm, P. Kienle, R. Zeller, R. Frahm, G. Materlik, Phys. Rev. Lett. 58 (1987) 737.
[28] G. Schütz, R. Wienke, W. Wilhelm, W. Wagner, P. Kienle, R. Zeller, R. Frahm, Z. Phys. B 75 (1989) 495.
[29] C.T. Chen, F. Sette, Y. Ma, S. Modesti, Phys. Rev. B 42 (1990) 7262.
[30] W.L. O'Brien, B.P. Tonner, Phys. Rev. B 50 (1994) 12672.
[31] M.G. Samant, J. Stöhr, S.S.P. Parkin, G.A. Held, B.D. Hermsmeier, F. Herman, M. van Schilfgaarde, L.-C. Duda, D.C. Mancini, N. Wassdahl, R. Nakajima, Phys. Rev. Lett. 72 (1994) 1112.
[32] W.L. O'Brien, B.P. Tonner, G.R. Harp, S.S.P. Parkin, J. Appl. Phys. 76 (1994) 6462.
[33] J. Hunter Dunn, D. Arvanitis, N. Mårtensson, M. Tischer, F. May, M. Russo, K. Baberschke, J. Phys.: Condens. Matter 7 (1995) 1111.
[34] S. Pizzini, A. Fontaine, C. Giorgetti, E. Dartyge, J.F. Bobo, M. Piecuch, F. Baudelet, Phys. Rev. Lett. 74 (1995) 1470.
[35] D. Weller, J. Stöhr, R. Nakajima, A. Carl, M.G. Samant, C. Chappert, R. Mégy, P. Beauvillain, P. Veillet, G. Held, Phys. Rev. Lett. 75 (1995) 3752.
[36] G.R. Harp, S.S.P. Parkin, W.L. O'Brien, B.P. Tonner, Phys. Rev. B 51 (1995) 12037.
[37] H.A. Dürr, G.Y. Guo, G. van der Laan, J. Lee, G. Lauhoff, J.A.C. Bland, Science 213 (1997) 277.
[38] B.T. Thole, P. Carra, F. Sette, G. van der Laan, Phys. Rev. Lett. 68 (1992) 1943.
[39] P. Carra, B.T. Thole, M. Altarelli, X. Wang, Phys. Rev. Lett. 70 (1993) 694.
[40] P. Carra, H. König, B.T. Thole, M. Altarelli, Physica B 192 (1993) 182.
[41] J. Stöhr, H. König, Phys. Rev. Lett. 75 (1995) 3748.
[42] H. Dürr, G. van der Laan, Phys. Rev. B 54 (1996) 760.
[43] G. van der Laan, J. Phys.: Condens. Matter 9 (1997) L259.
[44] G. van der Laan, Phys. Rev. B 57 (1998) 5250.
[45] G. van der Laan, Phys. Rev. B 57 (1998) 112.
[46] B.D. Cullity, Introduction to Magnetic Materials, Addison-Wesley, Reading, MA, 1972.
[47] F. Sette, C.T. Chen, Y. Ma, S. Modesti, N.V. Smith, in: S.S. Hasnain (Ed.), X-Ray Absorption Fine Structure, Ellis Horwood Limited, Chichester, England, 1991, p. 96.
[48] Y.U. Idzerda, L.H. Tjeng, H.-J. Lin, C.J. Gutierrez, G. Meigs, C.T. Chen, Phys. Rev. B 48 (1993) 4144.
[49] J. Stöhr, Y. Wu, B.D. Hermsmeier, M.G. Samant, G.R. Harp, S. Koranda, D. Dunham, B.P. Tonner, Science 259 (1993) 658.
[50] A. Aspelmeier, M. Tischer, M. Farle, M. Russo, K. Baberschke, D. Arvanitis, J. Magn. Magn. Mater. 146 (1995) 256.
[51] C.T. Chen, Y.U. Idzerda, H. Lin, G. Meigs, A. Chaiken, G.A. Prinz, G.H. Ho, Phys. Rev. B 48 (1993) 642.
[52] L.H. Tjeng, Y.U. Idzerda, P. Rudolf, F. Sette, C.T. Chen, J. Magn. Magn. Mater. 109 (1992) 288.
[53] W.L. O'Brien, B.P. Tonner, Phys. Rev. B 52 (1995) 1.
[54] J. Stöhr, Y. Wu, in: A.S. Schlachter, F.J. Wuilleumier (Eds.), New Directions in Research with Third-Generation Soft X-Ray Synchrotron Radiation Sources, Kluwer Academic Publishers, Netherlands, 1994, p. 221.
[55] J. Stöhr, J. Electron. Spectrosc. Relat. Phenom. 75 (1995) 253.
[56] J. Stöhr, R. Nakajima, IBM J. Res. Develop. 42 (1998) 73.
[57] O. Eriksson, B. Johansson, R.C. Albers, A.M. Boring, M.S.S. Brooks, Phys. Rev. B 42 (1990) 2707.
[58] P. Söderlind, O. Eriksson, B. Johansson, R.C. Albers, A.M. Boring, Phys. Rev. B 45 (1992) 12911.
[59] H. Ebert, J. Stöhr, S.S.P. Parkin, M. Samant, A. Nilsson, Phys. Rev. B 53 (1996) 16067.
[60] R.P. Feynman, R.B. Leighton, M. Sands, The Feynman Lectures on Physics, Vol. I, Part 2, Addison-Wesley, Reading, MA, 1964.
[61] J.C. Slater, G.F. Koster, Phys. Rev. 94 (1954) 1498.
[62] D.A. Papaconstantopoulos, Handbook of the Band Structure of Elemental Solids, Plenum, New York, 1986.
[63] G.H.O. Daalderop, P.J. Kelly, M.F.H. Schuurmans, Phys. Rev. B 50 (1994) 9989.
[64] P.F. Carcia, A.D. Meinholdt, A. Suna, Appl. Phys. Lett. 47 (1985) 178.

[65] J.E. Hurst Jr., W.J. Kozlovsky, Jpn. J. Appl. Phys. 32 (1993) 5301.
[66] G.H.O. Daalderop, P.J. Kelly, M.F.H. Schuurmans, Phys. Rev. B 44 (1991) 12054.
[67] D. Renard, G. Nihoul, Philos. Mag. B 55 (1987) 75.
[68] C. Cesari et al., J. Magn. Magn. Mater. 78 (1989) 296.
[69] J. Ferrè et al., Appl. Phys. Lett. 56 (1990) 1588.
[70] V. Grolier et al., Phys. Rev. Lett. 71 (1993) 3023.
[71] R. Nakajima, J. Stöhr, I. Idzerda, Phys. Rev. B 59 (1999) 6421.
[72] R. Nakajima, Ph. D. dissertation, Standford University, 1998, unpublished.
[73] H.J.G. Draaisma, W.J.M. de Jonge, J. Appl. Phys. 64 (1988) 3610.
[74] O. Eriksson, M.S.S. Brooks, B. Johansson, Phys. Rev. B 41 (1990) 7311.
[75] P. Strange, H. Ebert, J.B. Staunton, B.L. Gyorffy, J. Phys. C 1 (1989) 3947.
[76] L. Szunyogh, B. Újfalussy, P. Weinberger, Phys. Rev. B 51 (1995) 9552.
[77] G. Aubert, J. Appl. Phys. 39 (1968) 504.
[78] J.P. Rebouillat, IEEE Magn. 8 (1972) 630.
[79] P. Escudier, Ann. Phys. (Paris) 9 (1975) 125.
[80] R. Pauthenet, J. Appl. Phys. 53 (1982) 8187.
[81] F. Ducastelle, F. Cyrot-Lackmann, J. Phys. (Paris) C 1 (1971) 537.
[82] J. Smit, in: J. Smit (Ed.), Magnetic Properties of Materials, McGraw-Hill, New York, 1971, p. 1.
[83] B. Újfalussy, L. Szunyogh, P. Bruno, P. Weinberger, Phys. Rev. Lett. 77 (1996) 1805.
[84] I.V. Solovyev, P.H. Dederichs, I. Mertig, Phys. Rev. B 52 (1995) 13419.
[85] G. van der Laan, J. Phys.: Condens. Matter 10 (1998) 3239.
[86] H.A. Dürr, G. van der Laan, J. Vogel, M. Finazzi, J.B. Goedkoop, IEEE Trans. Magn. 34 (1998) 1201.
[87] A.N. Anisimov, M. Farle, P. Poulopoulos, W. Platow, K. Baberschke, P. Isberg, R. Wäppling, A.M.N. Niklasson, O. Eriksson, Phys. Rev. Lett. 82 (1999) 2390.
[88] O. Hjortstam, K. Baberschke, J.M. Wills, B. Johansson, O. Eriksson, Phys. Rev. B 55 (1997) 15026.
[89] A. Nilsson, J. Stöhr, T. Wiell, M. Aldén, P. Bennich, N. Wassdahl, M. Samant, S.S.P. Parkin, N. Mårtensson, J. Nordgren, B. Johansson, H.L. Skriver, Phys. Rev. B 54 (1996) 2917.
[90] S. Hüfner, in: L. Ley, M. Cardona (Eds.), Photoemission of Solids II, Springer Series in Topics in Applied Physics 27, Springer, Heidelberg, 1979, p. 173.
[91] A.R. Mackintosh, O.K. Andersen, in: M. Springford (Ed.), Electrons at the Fermi Surface, Cambridge University Press, Cambridge, 1980, p. 149.
[92] J. Michl, E.W. Thulstrup, Spectroscopy with Polarized Light, VCH Publishers, New York, 1995.
[93] J.D. Jackson, Classical Electrodynamics, Wiley, New York, 1962.
[94] H. Dürr, G. van der Laan, B.T. Thole, Phys. Rev. Lett. 76 (1996) 3464.
[95] W.A. Harrison, Electronic Structure and Properties of Solids, Freeman, San Francisco, 1980.
[96] C.J. Ballhausen, Molecular Electronic Structures of Transition Metal Complexes, McGraw-Hill, New York, 1979.